Tellus (2003), 55A, 61–87
Printed in UK. All rights reserved

TELLUS
ISSN 0280–6495

The effects of interactions between surface forcings in the development of a model-simulated polar low in Hudson Bay

By PHILIPPE GACHON[1*†], RENÉ LAPRISE[1], PETER ZWACK[1] and FRANÇOIS J. SAUCIER[2],
[1]*Department of Earth and Atmospheric Sciences, University of Quebec at Montreal, Montreal, Quebec, Canada;*
[2]*Maurice Lamontagne Institute, Ocean Sciences Branch, Department of Fisheries and Oceans, 850 route de la Mer, P.O. Box 1000, Mont-Joli (Qc), Canada G5H 3Z4*

(Manuscript received 29 November 2000; in final form 18 June 2002)

ABSTRACT

A 30-km version of the Canadian Regional Climate Model is used to simulate a polar low development in early December 1988 over the Hudson Bay. This polar low is quantitatively analyzed in detail, in the initial and mature stages of its development, in order to understand physically how sea surface conditions influence this mesocyclone. This analysis is realized via the description of the effects of different atmospheric forcings (i.e. thermal and vorticity advection, and turbulent and convective fluxes) on the polar low development (called the direct effects) using the diagnostic equations of omega and vorticity tendency. Also, the effects of forcing interactions on subsequent cyclone development (called the indirect effects) is analyzed via the diagnostic equations of vorticity and thermal advection tendencies. In the early stage of development, a low-level cyclogenesis appears over the northwestern Hudson Bay essentially due to diabatic forcings in the context of low-level cold air advection. Progressively, the synergetic effect of time rate of changes in advection terms, resulting from surface diabatic and stress forcings, favours low-level cyclogenesis and baroclinicity over open water near the sea-ice margin, whose shape is determinant for the deepening and tracking of the polar low. In the mature stage, the growth in advection terms becomes the main factor of cyclone intensification with the increase in low-level convection. Forcings are maximum near the surface and differ substantially from the vertical structure found in classical extratropical cyclones. In the upper troposphere they appear to play a secondary role in this polar low development. Finally, the polar low studied here is primarily the result of combined forcing interactions near the sea-ice edge, which are responsible for vorticity and thermal advection changes at low levels. It is also found that the indented sea-ice shape is a favourable factor for the local surface cyclogenesis due to the formation of local Laplacians of diabatic and thermal forcings.

1. Introduction

The trajectory and evolution of low-pressure systems (including polar lows) in the polar and subpolar basins appear to be closely linked to land–sea-ice–ocean contrasts within the seasonal sea-ice zone (Ledrew, 1984). In particular, the Canadian coastlines in Arctic and subarctic regions are more than 5000 km long, and are highly conducive to mesoscale cyclone formation, especially in autumn and winter when ocean/atmosphere exchanges are extreme. Polar lows are quite common in and near Canadian waters, occuring over the Beaufort Sea, Hudson Bay, Labrador Sea and Davis Strait (MEP Company, 1989). Over Hudson Bay, Roch et al. (1991) reported on a polar low that formed over an ice-free region in early December

*Corresponding author.
†Current affiliation: Maurice Lamontagne Institute. e-mail: gachonp@dfo-mpo.gc.ca

1988. They tested the sensitivity of the development of this polar low to horizontal resolution and sea-ice cover using the Canadian operational regional finite-element model (RFE). The most realistic simulation of the low was obtained in a simulation using a 25-km grid mesh, and the ice cover analysis of Environment Canada's Ice Centre. The importance of the open water for the formation of the simulated low was revealed by the failure of a closed low to form in the experiment with complete sea-ice cover over Hudson Bay. To expand the earlier results of Roch et al. (1991), Albright et al. (1995) used the MM4 mesoscale model of Pennsylvania State University-National Center for Atmospheric Research (PSU-NCAR), with a 20-km grid mesh and 28 sigma levels, in order to simulate this polar low over Hudson Bay. They made a set of experiments to test the sensitivity of the development to various prescriptions of the surface fluxes, condensation heating, sea-surface temperature and the configuration of the ice boundary. In their conclusions, Albright et al. (1995) state that this polar low developed as a consequence of latent heat release in organized deep convection that formed when an upper-level cold low moved over a relatively warm body of open water from which large fluxes of heat and moisture took place. Baroclinic forcing at high levels appeared to play little direct role in this low development. Instead, the configuration of the upstream ice boundary provided an important iniatiting and organizing mechanism.

These two sensitivity studies show clearly that the sea-ice and open-water distributions are important for the development of polar lows. However, the exact mechanism of how the polar low forms is only partly understood. In this paper, the principal objective is to study quantitatively with new diagnostic tools how sea-ice distribution leads to a mesoscale cyclone development. In addition to presenting the direct contributions of forcings such as temperature and vorticity advection, and heat, humidity and momentum fluxes on the development of the cyclone (i.e. on the vertical motion and vorticity tendency), interactions between the forcings are also analyzed. The effects of these forcing interactions on the subsequent cyclone development, called the indirect effects, are presented in term of diagnostic of advection terms tendencies due to all forcings. With the fuller diagnostic, we could precisely understand how the polar low evolves in time.

In section 2, the Canadian Regional Climate Model (CRCM) used to simulate the polar low development in the second week of December 1988 is briefly presented. In section 3, diagnostic equations are developed to study direct and indirect effects on polar low development. In section 4, the diagnostic budgets are discussed during the initial and mature stages of the polar low development, and physical interpretations are presented on the role of forcing interaction patterns near the surface during this mesoscale cyclogenesis. Further discussion is presented in section 5, with particular emphasis on the polar low dynamics and the influence of the shape and location of the sea-ice boundary on mesoscale atmospheric circulation. The final section provides a summary and the main conclusions.

2. Model and experiments

2.1. General description of the model

The CRCM model employs semi-implicit semi-lagragian numerical algorithms as described in Caya and Laprise (1999). It is based on the fully elastic non-hydrostatic Euler equations. The vertical coordinate of CRCM is built on a Gal-Chen terrain-following coordinate, and the model uses a staggered Arakawa C-grid in the horizontal, on a polar stereographic projection (Bergeron et al., 1994). In the simulation, the model was run with a 30-km grid mesh and 40 levels in the vertical. With this resolution, the timestep used here is 7.5 min. A one-way nested procedure is used to drive the CRCM with NCEP (National Centers of Environmental Prediction) reanalyses (2.5° lat × 2.5° long grid). These atmospheric data were available to us at 12 h intervals (0000 and 1200 UTC) on 12 pressure levels. Interpolations in time and in space were performed to supply initial and lateral atmospheric boundary conditions. Details of interpolation in time and in space, nesting and time filter are given in Caya (1996) and Caya and Laprise (1999).

This model version is used with the complete subgrid-scale physical parameterization of the second-generation Canadian Centre for Climate modelling and analysis General Circulation Model (CCCma GCM version II, described in McFarlane et al., 1992). Principal physical schemes regarding turbulent vertical transfer of heat, humidity and momentum near the surface are presented in Caya and Laprise (1999) and Morneau (1995). The details of other parameterizations (land surface scheme, cloud coverage and horizontal diffusion) and their coupling with the dynamics of the model may be found in Caya and Laprise (1999) and Caya (1996).

2.2. *General description of the simulation and experimental configuration*

The simulation is realized with two nested procedures. Firstly, an integration is conducted with a model of 30-km grid in the horizontal and 21 levels in the vertical between the surface and near 20 km. This run is nested by the NCEP reanalyses between 24 November and 16 December 1988. The spin-up run in the last week of November 1988 is realized to adjust the surface climatological fields according to atmospheric conditions. Secondly, between 6 and 11 December 1988, a new run is realized with the same horizontal resolution than the first but with 40 levels in the vertical (to increase the vertical resolution in the troposphere). This second run is nested by the first run with coarser vertical resolution. It constitutes the simulation used here to analyze the development of the polar low between 7 and 10 December. In the first run, the integration domain extends on an area of 18 $\times$ 10^6 km^2, centered over Hudson Bay, with a grid of 141 $\times$ 141 points in the horizontal. In the second run, the domain is slightly smaller with 131 $\times$ 131 points (shown without the sponge zone in Fig. 1). For the two runs, the topography is interpolated from a 1° lat $\times$ 1° long database of CCCma. Initial values of prognostic land surface variables of CRCM (ground temperature, snow amount and liquid and frozen soil water content) came from a 1° $\times$ 1° climatological database compiled at CCCma.

For sea surface temperature, the model uses monthly mean observational analyses derived from a 2° lat $\times$ 2° long AMIP (Atmospheric Model Intercomparison Project, Gates, 1992) data set. For the Great Lakes surface temperature, the prescribed values (constant for the entire surface of each of the Great Lakes) are derived from climatological monthly means, on the period 1951–1980 period for Michigan Lake and 1966–1988 for all the other Great Lakes (Irbe, 1992; Saulesleja, 1986). For sea-ice extent and thickness, AMIP data have been modified to produce the distribution of sea-ice shown in Fig. 1. This configuration of sea-ice cover differs somewhat from the observed ice cover (valid on 8 December 1988) shown in Figs. 7 and 8 of Roch et al. (1991). This ice distribution has been used for a more complete work of Gachon (1999) to study the role of sea-ice extent anomalies on the atmospheric mesoscale circulation over the month of December (not shown).

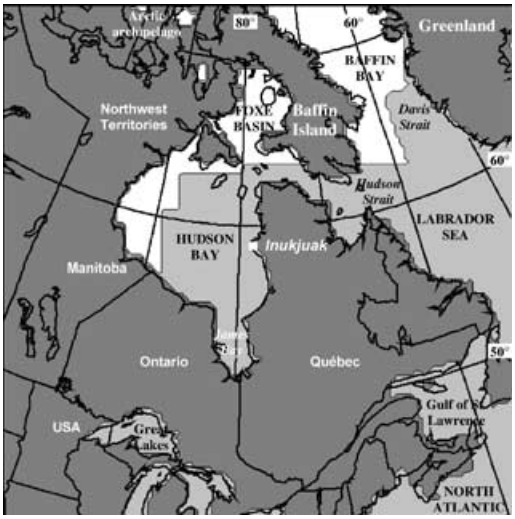

Fig. 1. Geographic reference map of the CRCM domain, excluding the lateral sponge zone, and ground cover used in the simulation. White color corresponds to sea-ice, light grey to open water (ocean or Great Lakes), and dark grey to continent.

3. Diagnostic methods

3.1. *Direct effects*

The direct effects of forcings are studied in part using a generalized omega equation in pressure coordinate, such as given in Zwack et al. (1996):

$$\left(\frac{pf}{R}(f+\zeta)\frac{\partial^2}{\partial p^2}+\nabla^2 S\right)\omega = -\nabla^2(-\vec{V}\cdot\vec{\nabla}T) - \nabla^2\frac{\dot{q}}{C_p}+\frac{pf}{R}\frac{\partial}{\partial p}[\vec{V}\cdot\vec{\nabla}(f+\zeta)] - \frac{pf}{R}\frac{\partial}{\partial p}(\hat{k}\cdot\vec{\nabla}\times\vec{F})-\frac{pf}{R}\frac{\partial}{\partial p}(\hat{k}\cdot\vec{\nabla}\times\vec{O}) + \frac{pf}{R}\omega\frac{\partial^2\zeta}{\partial p^2}+\frac{pf}{R}\frac{\partial}{\partial p}\left(\frac{\partial\omega}{\partial x}\frac{\partial v}{\partial p}-\frac{\partial\omega}{\partial y}\frac{\partial u}{\partial p}\right) \quad (1)$$

where p is the pressure, f the Coriolis parameter, R the gas constant for dry air, S the static stability, T the temperature, $\dot{q}$ the diabatic heating rate, ζ the relative vorticity, C_p the specific heat at constant pressure, F the friction term, O the orographic term, ω the vertical motion in pressure coordinate, and u and v the horizontal wind components in the x and y directions, respectively. The orographic term is defined from a specified profile of divergence due to a slope (using

the properties of wind in Ekman spiral), such as given in Desjardins (1993) and Tardif (1992).

On the right-hand side of eq. (1), the first five forcing terms represent the forcing due to: (i) the Laplacian of temperature advection (LTA); (ii) the Laplacian of the total diabatic heating due to sensible heat flux (LSH) and latent heat release (LLH), which also includes the divergence/convergence of the total condensation and convective heat flux (we have neglected the contribution of the radiative term); (iii) the vorticity advection (VA); (iv) the friction (F) and (v) the orography (O) terms. The last two terms are vertical advection of vorticity and tilting–twisting components, respectively. Equation (1) is an elliptic equation, and its solution requires boundary conditions. This equation was solved with the relaxation method (Haltiner and Williams, 1980; Desjardins, 1993), with $\omega = 0$ being imposed on all (lateral, upper and lower) boundaries. In order to avoid problems with the occasional occurrence of neutral stability ($S = 0$), S has been assigned a minimum value of 1×10^{-5} K Pa^{-1}. In solving for the vertical motion by relaxation, each iteration allows one to calculate a value for omega, and this value is issued to recompute the right-hand side terms of eq. (1) which contain omega (in the vertical advection and tilting–twisting terms) at the time of the next iteration. With this iterative procedure, the solution converges if these terms are small or the sum of these two terms is relatively weak, which is the case in the polar low development studied here. With eq. (1), the contributions of the six forcing terms could be calculated separately because the left-hand side is linear with respect to ω, provided that homogeneous boundary conditions are used.

Equation (1) has been derived assuming hydrostatic equilibrium and with the assumption that the vertical variation of vorticity tendency equals its geostrophic counterpart (Gachon, 1999). In general, at mesoscale, the vorticity tendency is not similar to geostrophic one, particularly in the boundary layer where the ageostrophic component of vorticity is not negligible. However, the vertical variation of these two tendencies is relatively similar (as shown in Fig. 13), and hence this hypothesis is an accurate simplification in order to have an appropriate diagnostic of ω.

The lower boundary condition $\omega = 0$ in eq. (1) is not adequate in mountainous regions, where vertical motion near the surface may be strong. However, in the case of the marine cyclone which is the major focus in this study, this approximation is not expected to be a serious source of error.

The contributions to vertical motion obtained from eq. (1) can then be combined with the vorticity equation in isobaric coordinates, in the following form:

$$\frac{\partial \zeta}{\partial t} = -\vec{V} \cdot \vec{\nabla}(f+\zeta) + (f+\zeta)\frac{\partial \omega}{\partial p} - \omega \frac{\partial \zeta}{\partial p} - \left(\frac{\partial \omega}{\partial x}\frac{\partial v}{\partial p} - \frac{\partial \omega}{\partial y}\frac{\partial u}{\partial p}\right) + (\hat{k} \cdot \vec{\nabla} \times \vec{F}) + (\hat{k} \cdot \vec{\nabla} \times \vec{O}). \quad (2)$$

Six components of vorticity tendency are obtained:

$$\frac{\partial \zeta}{\partial t} = \left[\frac{\partial \zeta}{\partial t}\right]_{\mathrm{VA}} + \left[\frac{\partial \zeta}{\partial t}\right]_{\mathrm{F}} + \left[\frac{\partial \zeta}{\partial t}\right]_{\mathrm{O}} + \left[\frac{\partial \zeta}{\partial t}\right]_{\mathrm{LTA}} + \left[\frac{\partial \zeta}{\partial t}\right]_{\mathrm{LSH}} + \left[\frac{\partial \zeta}{\partial t}\right]_{\mathrm{LLH}} \quad (3)$$

where the subscripts follow the convention used above in eq. (1). These components are defined as:

$$\left[\frac{\partial \zeta}{\partial t}\right]_{\mathrm{VA}} = -\vec{V} \cdot \vec{\nabla}(f+\zeta) + (f+\zeta)\frac{\partial \omega_{\mathrm{VA}}}{\partial p} - \omega_{\mathrm{VA}}\frac{\partial \zeta}{\partial p} - \left(\frac{\partial \omega_{\mathrm{VA}}}{\partial x}\frac{\partial v}{\partial p} - \frac{\partial \omega_{\mathrm{VA}}}{\partial y}\frac{\partial u}{\partial p}\right) \quad (4)$$

$$\left[\frac{\partial \zeta}{\partial t}\right]_{\mathrm{F}} = \hat{k} \cdot \vec{\nabla} \times \vec{F} + (f+\zeta)\frac{\partial \omega_{\mathrm{F}}}{\partial p} - \omega_{\mathrm{F}}\frac{\partial \zeta}{\partial p} - \left(\frac{\partial \omega_F}{\partial x}\frac{\partial v}{\partial p} - \frac{\partial \omega_{\mathrm{F}}}{\partial y}\frac{\partial u}{\partial p}\right) \quad (5)$$

$$\left[\frac{\partial \zeta}{\partial t}\right]_{\mathrm{O}} = \hat{k} \cdot \vec{\nabla} \times \vec{O} + (f+\zeta)\frac{\partial \omega_{\mathrm{O}}}{\partial p} - \omega_{\mathrm{O}}\frac{\partial \zeta}{\partial p} - \left(\frac{\partial \omega_{\mathrm{O}}}{\partial x}\frac{\partial v}{\partial p} - \frac{\partial \omega_{\mathrm{O}}}{\partial y}\frac{\partial u}{\partial p}\right) \quad (6)$$

and

$$\left[\frac{\partial \zeta}{\partial t}\right]_{\mathrm{T}} = (f+\zeta)\frac{\partial \omega_{\mathrm{T}}}{\partial p} - \omega_{\mathrm{T}}\frac{\partial \zeta}{\partial p} - \left(\frac{\partial \omega_{\mathrm{T}}}{\partial x}\frac{\partial v}{\partial p} - \frac{\partial \omega_{\mathrm{T}}}{\partial y}\frac{\partial u}{\partial p}\right), \quad \text{where T = LTA, LSH or LLH.} \quad (7)$$

In eqs. (4)–(6), kinematic forcings (VA, F and O) act directly on vorticity tendency and via vertical motion. The thermodynamic terms in eq. (7) act only via the influence of vertical motion. Recently, an equation similar to eq. (2) has been used with success by

Räisänen (1997, 1995) to analyse different contributions for extratropical cyclone explosive development.

Using the hypsometric relation, the geopotential height tendency can be calculated at every pressure level:

$$\left[\frac{\partial \Phi}{\partial t}\right]_p = R\left[\int_p^{p_s} \frac{\partial T}{\partial t}\frac{\mathrm{d}p}{p} + \left(\frac{T_s}{p_s}\frac{\partial p_s}{\partial t}\right)\right] \tag{8}$$

where Φ is the geopotential height and the indice s refers to surface. In eq. (8), the temperature tendency is calculated with the thermodynamic relationship, and by using eq. (1), it is also possible to get six different contributions to temperature tendency (Gachon, 1999). To diagnose the surface pressure tendency in eq. (8), the following quasi-geostrophic relation is used:

$$\left[\frac{\partial \zeta_g}{\partial t}\right]_s = \frac{R}{f}\nabla^2\left(\frac{T_s}{p_s}\frac{\partial p_s}{\partial t}\right) \tag{9}$$

where ζ_g is the geostrophic vorticity calculated with an extended version of Zwack–Okossi equation (Zwack et al., 1996). With this equation, the different contributions to pressure tendency can be calculated using a relaxation method. With eqs. (8) and (9), six components of geopotential tendency are obtained:

$$\frac{\partial \Phi}{\partial t} = \left[\frac{\partial \Phi}{\partial t}\right]_{\mathrm{VA}} + \left[\frac{\partial \Phi}{\partial t}\right]_{\mathrm{F}} + \left[\frac{\partial \Phi}{\partial t}\right]_{\mathrm{O}} + \left[\frac{\partial \Phi}{\partial t}\right]_{\mathrm{LTA}} + \left[\frac{\partial \Phi}{\partial t}\right]_{\mathrm{LSH}} + \left[\frac{\partial \Phi}{\partial t}\right]_{\mathrm{LLH}}. \tag{10}$$

The system (1)–(7) will be used in section 4 to analyse the direct effets of different forcings in polar low development. Attention will be focused on the diagnostic of vertical motion and vorticity tendency. The height tendency equations (8)–(10) are used as an aid in the diagnosis of the indirect effects discussed below.

In order to analyse indirect effects of forcings in cyclogenesis, i.e. the influence of forcing interactions on subsequent cyclone development, the next subsection presents the diagnostic equation system developed for this purpose.

3.2. *Indirect effects*

In this section, two new equations are developed to analyze forcing interactions. Diagnostic equations are derived to calculate the tendency of advection terms (VA and LTA), separated into the different forcing contributions in a similar manner to that used for the direct effects. In pressure coordinates, the tendency of vorticity advection can be writen as:

$$\frac{\partial}{\partial \mathrm{t}}(-\vec{\mathrm{V}}\cdot\vec{\nabla}_{\mathrm{p}}\zeta) = -u\frac{\partial}{\partial x}\left(\frac{\partial \zeta}{\partial t}\right) - v\frac{\partial}{\partial y}\left(\frac{\partial \zeta}{\partial t}\right) - \frac{\partial u}{\partial t}\frac{\partial \zeta}{\partial x} - \frac{\partial v}{\partial t}\frac{\partial \zeta}{\partial y}. \tag{11}$$

In the first two terms on the right-hand side, vorticity tendency can be diagnosed with eq. (3). In order to calculate local wind tendency in the last two terms on the right-hand side in eq. (11), the quasi-geostrophic balance is used to calculate the wind acceleration from the evolution of the geopotential field. In the balanced state, the evolution of the wind is proportional to the variation of the geostrophic component. Firstly, the tendency of the geostrophic component can be inferred directly from the atmospheric mass redistribution:

$$\frac{\partial \vec{V}_g}{\partial t} = -\frac{1}{f}\vec{\nabla}\left(\frac{\partial \Phi}{\partial t}\right)\times\vec{\mathrm{k}}, \tag{12}$$

where the geopotential height tendency is diagnosed with eq. (10). Secondly, the wind tendency is assumed to be proportional to the geostrophic tendency, and can thus be deduced from the following approximation:

$$\frac{\partial \vec{V}}{\partial t} \approx R\frac{\partial \vec{V}_g}{\partial t} = R\left[-\frac{1}{f}\vec{\nabla}\left(\frac{\partial \Phi}{\partial t}\right)\times\vec{k}\right]. \tag{13}$$

Near the surface, the ageostrophic component of the wind becomes important and the wind tendency is smaller than the geostrophic one ($R < 1$). As shown in Fig. 14, the wind tendency is strongly correlated with the geostrophic counterpart. At low levels, the ageostrophic circulation is essentially due to turbulence, surface stress and/or convective processes. Consequently, the proportionality factor R in eq. (13) is a function of these processes and varies according to the distribution of turbulence intensity. This factor was calculated at every grid point, every level and every time step. As a first approximation, R was assumed identical for every forcing as in Gachon (1999), which appears to provide an acceptable approximation, as shown below.

With the eq. (13), the local wind tendency can be calculated using the height tendency from eq. (10), further divided to the contributions of different forcings, as follows:

$$\frac{\partial \vec{V}}{\partial t} = \left[\frac{\partial \vec{V}}{\partial t}\right]_{\mathrm{VA}} + \left[\frac{\partial \vec{V}}{\partial t}\right]_{\mathrm{F}} + \left[\frac{\partial \vec{V}}{\partial t}\right]_{\mathrm{O}} + \left[\frac{\partial \vec{V}}{\partial t}\right]_{\mathrm{LTA}} + \left[\frac{\partial \vec{V}}{\partial t}\right]_{\mathrm{LSH}} + \left[\frac{\partial \vec{V}}{\partial t}\right]_{\mathrm{LLH}}. \quad (14)$$

Using eqs. (3) and (14), it is possible to diagnose the tendency of vorticity advection [eq. (11)] from the following relation :

$$\frac{\partial}{\partial \mathrm{t}}(-\vec{\mathrm{V}} \cdot \vec{\nabla}_{\mathrm{p}}\zeta) = \sum \frac{\partial}{\partial \mathrm{t}}(-\vec{\mathrm{V}} \cdot \vec{\nabla}_{\mathrm{p}}\zeta)_{\mathrm{x}}$$

$$X = (\mathrm{VA}, \mathrm{F}, \mathrm{O}, \mathrm{LTA}, \mathrm{LSH}, \mathrm{LLH}). \quad (15)$$

In this equation, the gradient of vorticity is inferred directly from the simulated wind or vorticity.

For diagnosing the tendency of LTA, the following relation is used:

$$\nabla_{\mathrm{p}}^2 \frac{\partial}{\partial \mathrm{t}}(-\vec{\mathrm{V}} \cdot \vec{\nabla}_{\mathrm{p}}\mathrm{T}) = \nabla_{\mathrm{p}}^2 \left[-u\frac{\partial}{\partial x}\left(\frac{\partial T}{\partial t}\right) - v\frac{\partial}{\partial y}\left(\frac{\partial T}{\partial t}\right) - \frac{\partial u}{\partial t}\frac{\partial T}{\partial x} - \frac{\partial v}{\partial t}\frac{\partial T}{\partial y}\right]. \quad (16)$$

By using the diagnostic of temperature change according to the contributions of all forcings and eq. (14), the tendency of the Laplacian of thermal advection can be evaluated as:

$$\nabla_{\mathrm{p}}^2 \frac{\partial}{\partial \mathrm{t}}(-\vec{\mathrm{V}} \cdot \vec{\nabla}_{\mathrm{p}}\mathrm{T}) = \sum \nabla_{\mathrm{p}}^2 \frac{\partial}{\partial t}(-\vec{\mathrm{V}} \cdot \vec{\nabla}_{\mathrm{p}}T)_{\mathrm{x}},$$

$$X = (\mathrm{VA}, \mathrm{F}, \mathrm{O}, \mathrm{LTA}, \mathrm{LSH}, \mathrm{LLH}). \quad (17)$$

A positive Laplacian of thermal advection corresponds usually in our case to a local maximum of cold air advection, which tends to induce sinking motion and therefore low-level divergence, which further favors anticyclogenesis. This remark is valid in general but, as we will see in the following, the effects of LTA on the vertical motion and cyclogenesis is also due to the vertical distribution of the thermal advection.

In all diagnostic equations described above, the diabatic and friction terms are issued directly from the CRCM outputs (accumulated over 3 h periods). The LSH term comes from the heating rate associated with turbulent vertical diffusion, the LLH term from the heating rate associated with convection, and the F term from the wind tendency (u and v components) associated to vertical diffusion of momentum and gravity wave drag. The LLH term includes the convergence/divergence of the total condensation and convective heat flux. The details of numerical methods used to resolve this set of diagnostic equations are described in Gachon (1999) and Zwack et al. (1996). In the following, the orographic term O will be absent from the analysis because it is negligible in the polar low development.

By using the diagnostic equations (15) and (17), the influence of different forcings on the evolution of the vorticity and thermal advection terms can be analyzed in detail. In this way we will be able to gain insight into the physical processes induced by the interactions between forcings, and particularly the indirect effects associated with the turbulent fluxes of heat, humidity and momentum over open water. Therefore, in the following, the term cyclogenesis refers to a positive vorticity tendency and anticyclogenesis to a negative one.

4. Diagnostic analysis of a polar low development

4.1. General description of the polar low

The case studied here is a polar low developing over open water in Hudson Bay, and it is associated with large surface diabatic fluxes. As noted in the introduction, this polar low has also been investigated by Roch et al. (1991) and Albright et al. (1995). To complete these previous works, we further analyse here the role of forcing interactions on the low development. In Fig. 2 we see the evolution of the mean sea level pressure at Inukjuak in eastern Hudson Bay (cf. Fig. 1) during the development phase of this low, between 7 and 10 December 1988, in the simulation using the sea-ice cover shown in Fig. 1. The evolution of the simulated SLP is in relatively good agreement with SLP observed at this station. This low was absent in a simulation with complete sea-ice cover in Hudson Bay (e.g. Gachon 1999; Albright et al., 1995).

Prior to the development of the polar low over Hudson Bay, an intense extratropical cyclone moved off the coast of Labrador at 0700 UTC 8 December (Fig. 3a). The moving of this first low toward the Labrador Sea explains the growth in SLP in the first 30 h of the simulation at Inukjuak (shown in Fig. 2). This synoptic cyclone is associated with a baroclinic zone at 500 hPa over eastern Quebec (Fig. 3b). To the northwest of this surface low, cold and dry air was advected at low levels over the Hudson Strait and the northern Hudson Bay (see wind vectors and isotherms in Fig. 3a). A secondary surface trough began to

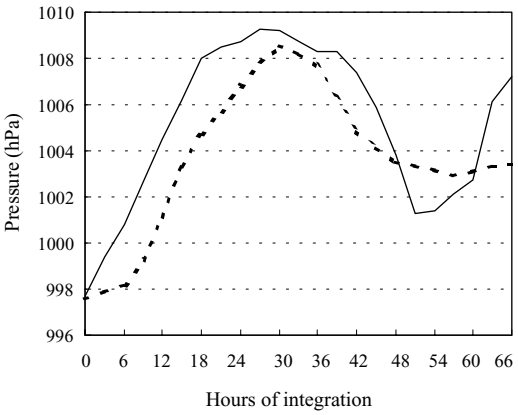

Fig. 2. Time series of the mean sea level pressure (SLP) extracted for Inukjuak (every 3 h) for 66 h starting 0600 UTC 7 December 1988, and ending 0000 UTC 10 December 1988. The solid line is the observed SLP and the dashed line is the simulated SLP. The observed values come from the meteorological station of Environment Canada at Inukjuak (Québec) shown in Fig. 1

develop from Inukjuak sector toward the northwestern Hudson Bay associated with a short-wave trough and weak cold air advection at 500 hPa (Fig. 3b). In all stages of development, temperature and vorticity advections were maximum near the surface and were weak above 700 hPa.

At 0700 UTC 9 December, the polar low is well formed over the Hudson Bay and has reached its mature stage (shown in Fig. 3c). The temperature gradients and winds near the surface are increased along the sea-ice edge and coastlines of western Hudson Bay compared to 24 h earlier (Fig. 3a). At 500 hPa, the short-wave trough is aligned on a meridional axis across the Bay (Fig. 3d), and induces a strong vorticity advection. After this time, the cylone deepens until 1800 UTC the same day. At this time, the absolute vorticity at 1000 hPa and the surface-sensible heat flux over Hudson Bay are maximum, around 80×10^{-5} s^{-1} and 1130 W m^{-2} respectively, the strongest upward motion occurs (peak values of around 5 Pa s^{-1} between 850 and 800 hPa, i.e., of the order of 0.5 m s^{-1}) and the winds at 1000 hPa reach the values of 25 m s^{-1}. The minimum surface pressure over the Bay remains constant at around 1001 hPa after this time (not shown). At Inukjuak the minimum of surface pressure of 1000.7 hPa was recorded at 1100 UTC 9 December (as shown in Fig. 2 between 48 and 54 h) and the surface winds of 25 m s^{-1} at 1300 UTC (e.g. Roch et al., 1991). The evolution of the surface pressure in our case resembles the HB10 case in Albright et al. (1995) obtained with an enlarged sea and a straight ice-edge (see their Fig. 11), but with quite a similar structure to their control run (see their Fig. 4b at 1800 UTC 9 December). However, in our case, the SST in Hudson Bay is at the freezing point of sea water (i.e. -1.8 °C), reducing the surface sensible heat fluxes and consequently the deepening of the polar low, compared to the case of Albright et al. (1995), where the SST is at 0 °C (SLP minimum of 997 hPa in their control run compared to 1001 hPa in our case). After reaching maturity, the polar low moved to the south of the Bay and slowly dissipated. This system disappeared definitively over James Bay around 0400 UTC 11 December.

In the next subsections we will analyze the polar low during the initial and mature stages, between 0400 and 0700 UTC 8 December, and at 0700 UTC 9 December, respectively, in order to understand cyclogenesis intensification. We will study the indirect and direct effects at 1000 hPa, where the cyclogenesis is maximum at 0700 UTC 8 December. The analysis is oriented firstly on the spatial distribution (in horizontal) of the temperature changes, and the vorticity and temperature advection tendencies according to all atmospheric forcings, at 0400 UTC 8 December. This allows us to gain insight into why the distribution of advection terms is progressively organized. Secondly, at the same time, the vertical structure of the changes in these two advection terms is also studied with the profile of omega and vorticity tendency in order to obtain a complete three-dimensional view of the polar low. Finally, we can exactly deduce how and why the vertical motion and vorticity tendency will be modified 3 h after, by changes in advection terms previously analyzed. At 0700 UTC 9 December we will also analyze the direct effects at the mature stage, in the sector of the maximum of surface cylogenesis and low-level upward motion. At this time, we will only focus on these two last terms, both in horizontal and vertical patterns. For all the figures presented in the following, the prognostic values correspond to the fields obtained from the archived CRCM simulation, and the diagnostic values to the fields obtained from the diagnostic equations presented in section 3.

4.2. Indirect and direct effects of forcings on cyclogenesis during the initial stage

4.2.1. Spatial distribution in horizontal. At the beginning of the development (0400 UTC 8 December)

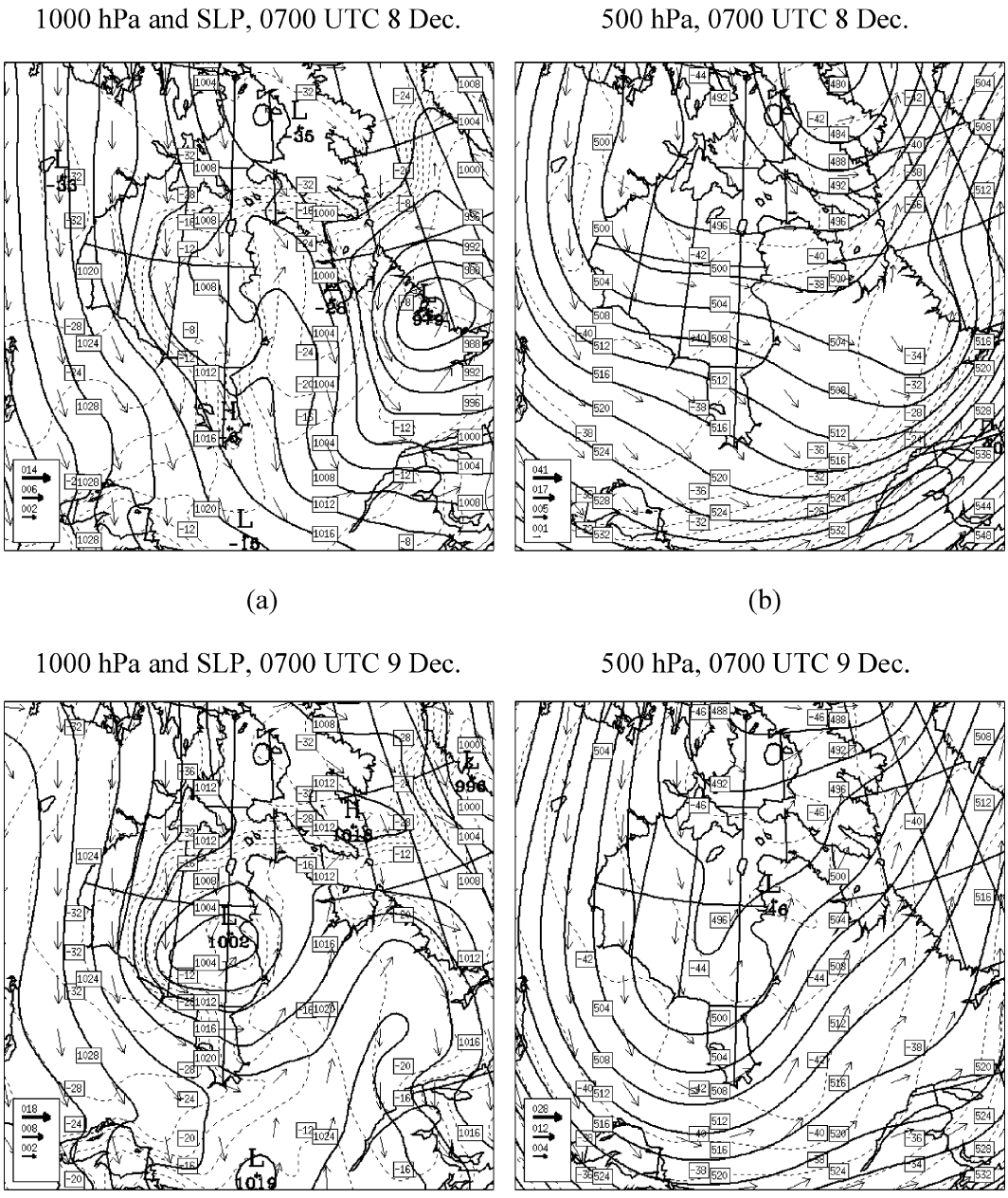

Fig. 3. Simulated synoptic fields at two stage of polar low development over Hudson Bay: (a) and (b) at 0700 UTC 8 December 1988; (c) and (d) 0700 UTC 9 December 1988. (a) and (c) SLP (every 4 hPa), 1000 hPa temperature (every 4 °C) and wind (in m s^{-1}); (b) and (d) 500 hPa geopotential height (every 4 dam), temperature (every 2 °C), and wind (in m s^{-1}). SLP and geopotential height are in solid line, temerature in dashed line and wind as arrows.

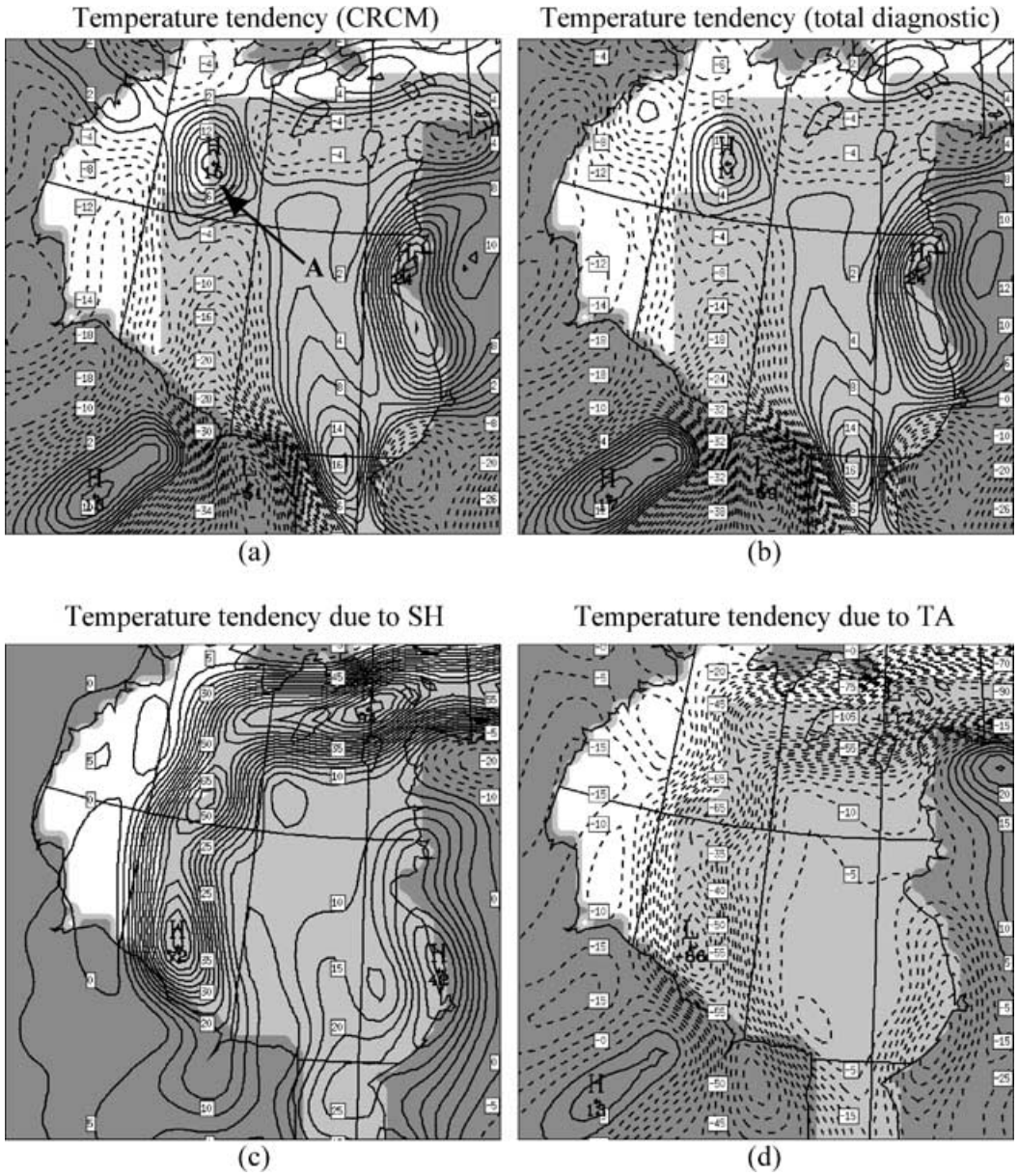

Fig. 4. 1000 hPa prognostic and diagnostic of temperature tendencies at 0400 UTC 8 December 1988 over Hudson Bay: (a) and (b) prognostic and total diagnostic of temperature tendency respectively (every 2×10^{-5} K s^{-1}); (c), and (d) temperature tendencies due to sensible heat flux (SH, every 5×10^{-5} K s^{-1}), and to temperature advection (TA, every 5×10^{-5} K s^{-1}), respectively. Solid and dashed lines are used for positive and negative values, respectively. Gray scale is ground cover defined in Fig. 1. Point A refers to the maximum in vorticity tendency in the next 3 h.

the 1000 hPa temperature tendency increases in the northwestern and eastern part of the Bay (Figs. 4a and 4b; the prognostic and diagnostic values are quite similar). As shown in Figs. 4c and 4d, this low-level warming is essentially due to the sensible heat flux from the open water along the sea-ice edge and coastline (solid line in Fig. 4), in association with the low-level cold air advection (dashed line in Fig. 4). At the same time,

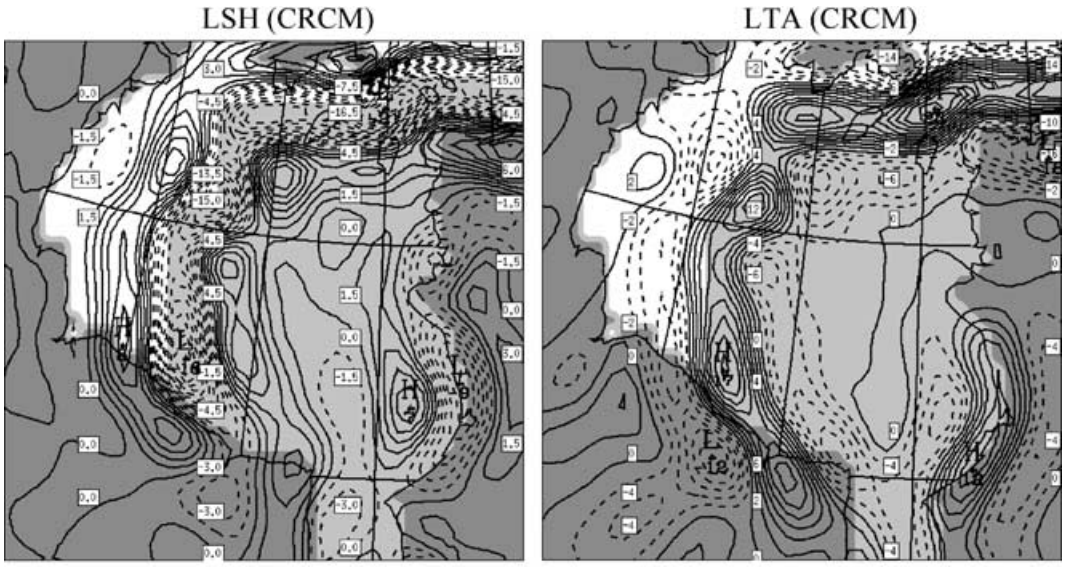

Fig. 5. Same time as Fig. 4 but for 1000 hPa prognostic Laplacian of diabatic and thermal forcing: (a) Laplacian of sensible heat flux (LSH) and (b) Laplacian of temperature advection (LTA). LSH and LTA are every 1.5 and 2×10^{-14} K m^{-2} s^{-1}, respectively.

the 1000 hPa vorticity advection is negative over open water, with two bands of positive values over sea-ice and near the sea-ice limit in the western Hudson Bay (not shown).

As can be seen in Figs. 5a and 5b, the spatial discontinuity of surface sensible heat flux associated with the ice border shape favors the formation of the Laplacian of diabatic or thermal forcings. Along the sea-ice edge or coastline, the negative values of the Laplacian of the diabatic term (i.e. maximum heating due to the surface sensible flux) are co-located with the positive values of the thermal Laplacian (i.e. the maximum cooling due to cold air advection). In the northwestern Hudson Bay, the negative thermal Laplacian over sea ice corresponds to a local minimum of cold air advection or a maximum zone of warming due to the advection of air warmed by surface diabatic fluxes from the open-water sector located close to the east.

As confirmed in Figs. 6 and 7, the shape of the open-water distribution had a strong influence on the pattern of the advection term tendencies at 1000 hPa. In Fig. 6 diagnostic tendencies of vorticity advection (VA) from eq. (15) are shown. In spite of some quantitative differences between the diagnostic VA tendency and the CRCM prognostic one, a good correlation appears between these two over Hudson Bay (Figs. 6a and 6b). In detail, the tendency of VA due to LSH is characterized by a symetric structure of negative and positive tendencies along the sea-ice edge and the coastline in the northern and western parts of Hudson Bay. Typically, LSH tends to decrease vorticity advection toward sea-ice or continent, and to increase vorticity advection over open water (Fig. 6c). For LLH forcing, a similar contribution appears near the sea-ice edge, but the positive tendency is less pronounced than for the sensible heat flux forcing (Fig. 6d). In the early stage of cyclogenesis, convection is weak and is confined to the low levels; consequently the LLH term in the VA tendency is weak at this time. As indicated in Fig. 6e, the tendency of VA due to LTA has an opposite structure to the sensible heating tendency. The concave indentation of the sea-ice cover in northwestern Hudson Bay creates a dipole of VA tendency, with positive values juxtaposed near negative values according to the distribution of oceanic heat fluxes. In fact, the positive values of VA are sometimes superimposed on the LSH tendency, as we will see in the following. The tendency of VA due to vorticity advection is essentially located along the western part of the Bay (Fig. 6f), with a dipole of positive values surrounding a negative

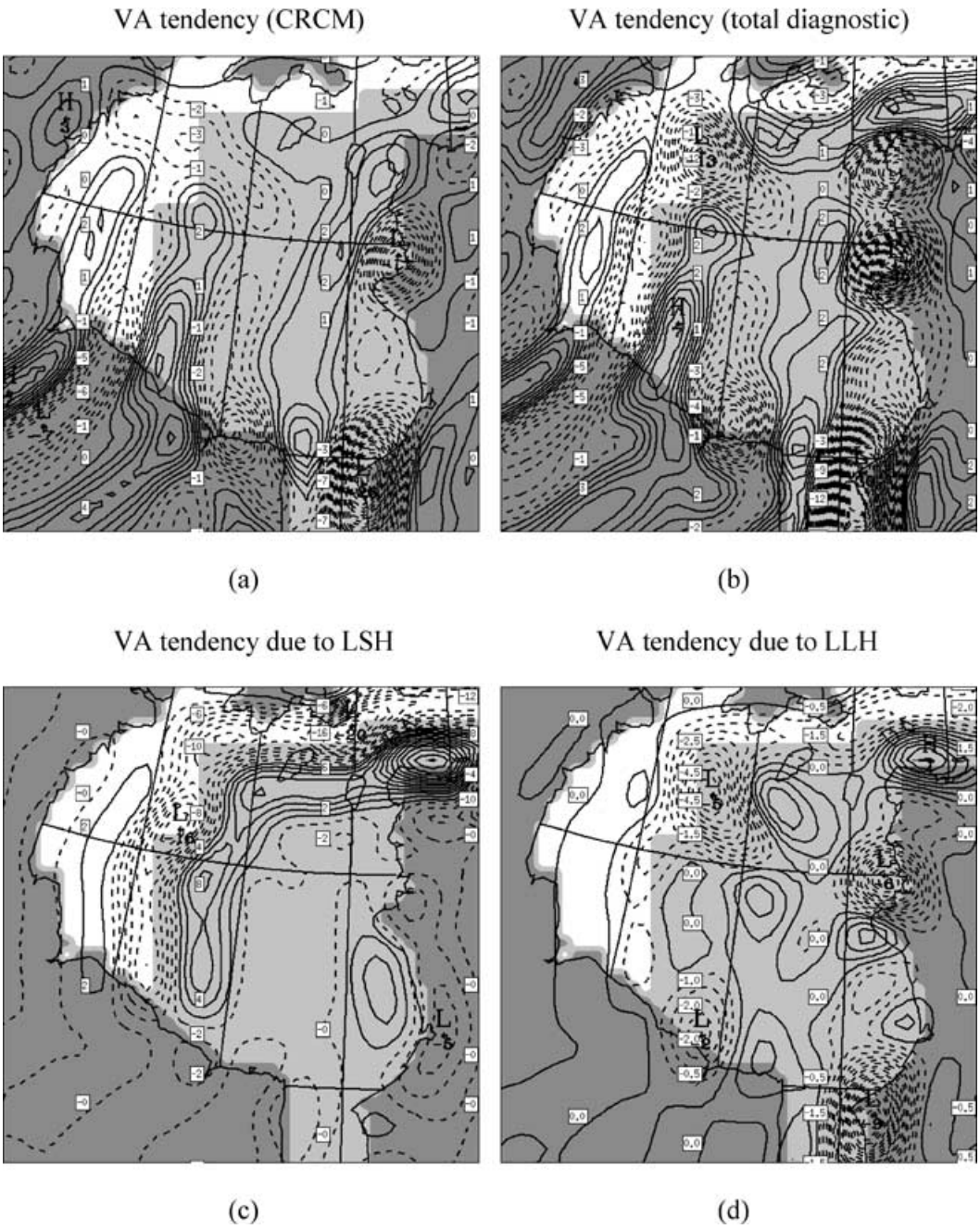

Fig. 6. Same time as Fig. 4 but for 1000 hPa prognostic and diagnostic tendencies of VA: (a) and (b) prognostic and total diagnostic tendency of VA, respectively (every 1×10^{-13} s^{-3}); (c), (d), (e), (f), and (g) tendency of VA due to LSH (every 2×10^{-13} s^{-13}), to LLH (every 0.5×10^{-13} s^{-3}), to LTA (every 2×10^{-13} s^{-3}), to VA (every 1×10^{-13} s^{-3}), and to F (every 1×10^{-13} s^{-3}), respectively.

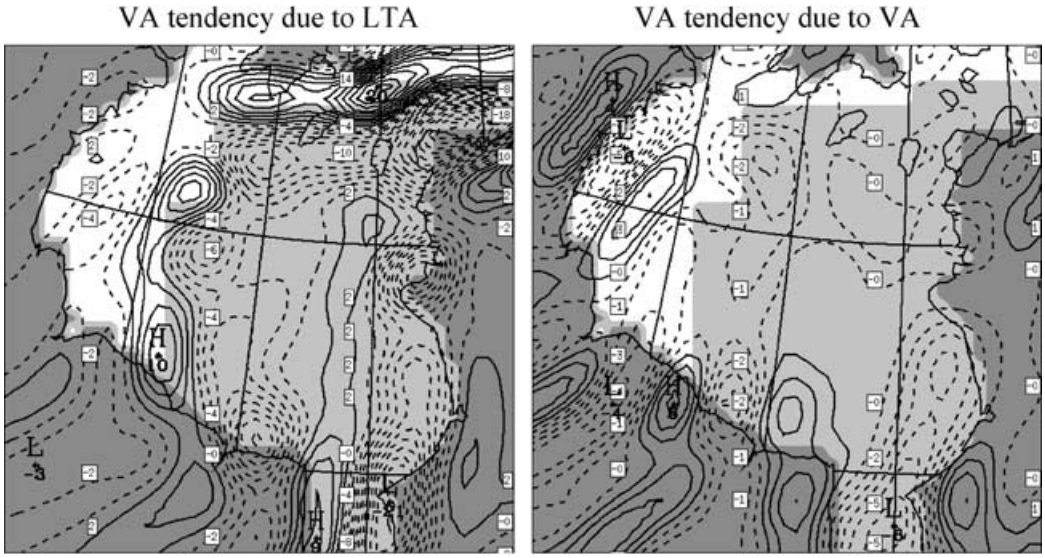

(e) (f)

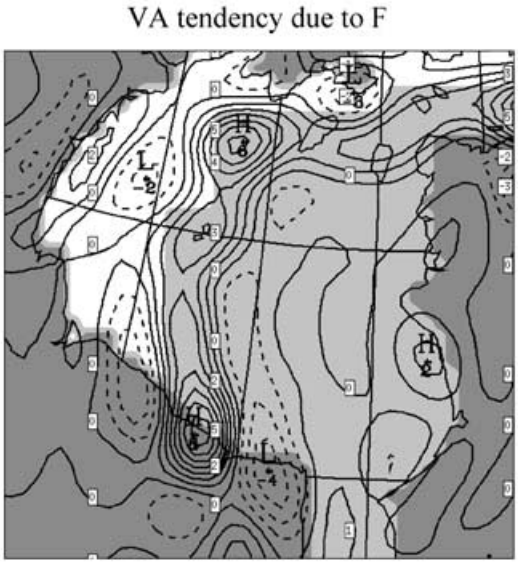

(g)

Fig. 6. (cont'd).

zone associated with the motion of a short-wave trough at 500 hPa (as shown 3 h after this time in Fig. 3b) and below this level. Finally, the tendency of VA due to friction is also positive over open water, along the sea-ice edge, and negative over sea ice or continent (Fig. 6g). Near the sea-ice boundary in northwestern Hudson Bay, the positive value due to momentum flux is superimposed on the LSH tendency values (Fig. 6c).

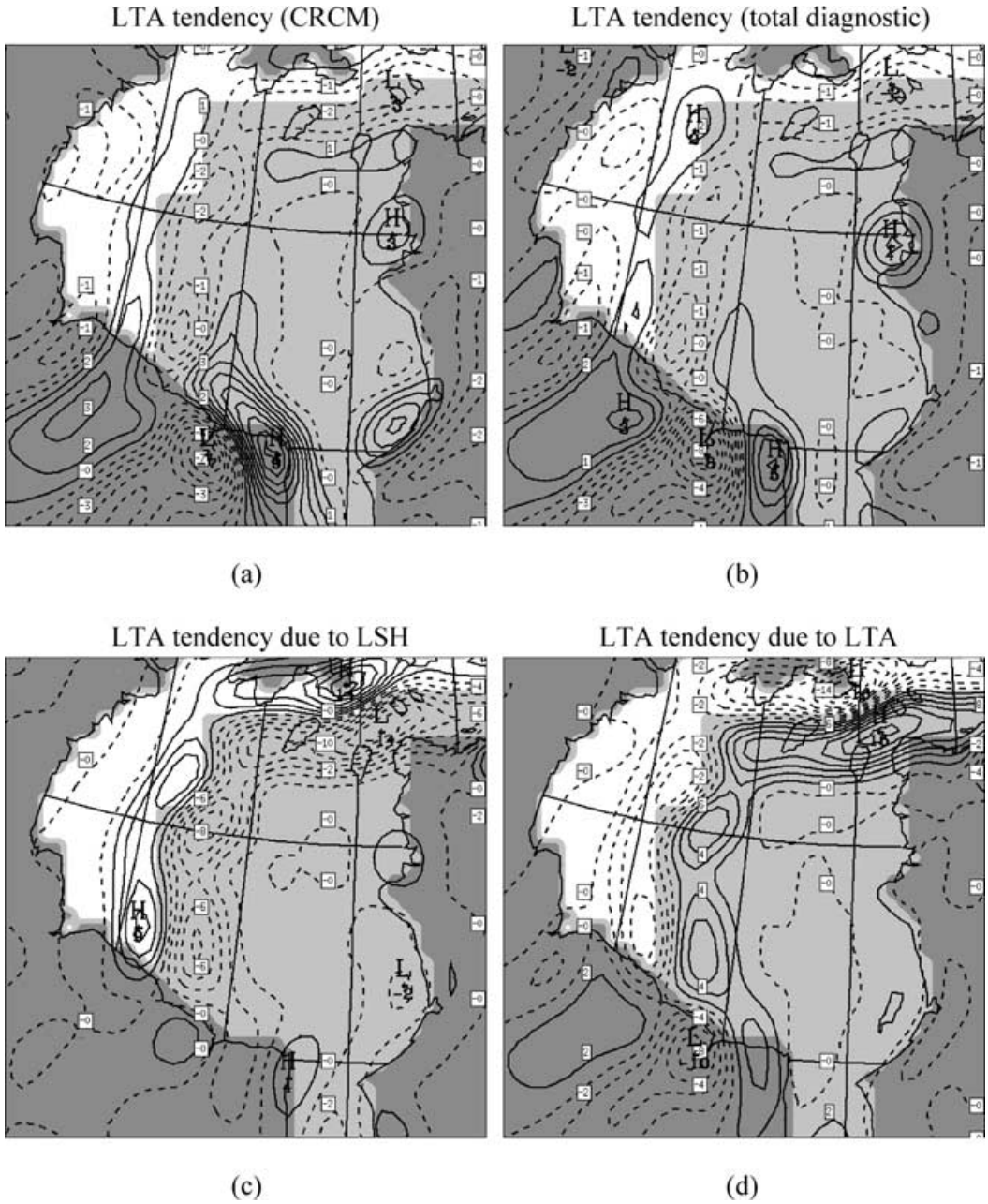

Fig. 7. Same as Figs 6 (a–e) but for the 1000 hPa LTA tendencies: (a) and (b) contours at every 1×10^{-17} K m^{-2} s^{-2}, (c) and (d) every 2×10^{-17} K m^{-2} s^{-2}.

In Fig. 7 diagnostic tendencies of the Laplacian of temperature advection from eq. (17) are shown. As revealed in Figs. 7a and 7b, the total diagnostic of LTA tendency is in good agreement with the CRCM prognostic one. In the northwest, a zone of maximum decrease in LTA tendency, just to the south of the indentation of the sea-ice outline, is partly juxtaposed on the increasing zone of VA (Figs. 6a and 7a). As

illustrated in Fig. 7c, the LTA tendency at 1000 hPa due to LSH is closely confined near the ice-free ocean, with a positive tendency of LTA along the sea-ice margin and coastlines, and negative values over open water. This reduction of LTA is more pronounced over open water, with the cumulative effect due to the divergence of convective heat flux near the surface (not shown). The role of thermal advection on the tendency in LTA is opposite to diabatic terms, with a decrease in LTA along the sea-ice margin and coastlines, and an increase in LTA over open water (cf. Fig. 7d with Fig. 7c). The effects of dynamic forcings (VA and F) on LTA change are negligible (not shown) compared to other forcings. Finally, the cumulative effect of LSH and LLH in the northwest near the sea-ice margin is responsible for the large decrease of LTA tendency in this sector, in spite of strong cold air advection over open water.

4.2.2. Vertical structure. At the same time, Fig. 8 shows the vertical structure of omega and tendencies of vorticity, VA and LTA at point A (refer to Fig. 4a). A weak upward motion occurs between 900 and 600 hPa (maximum at 830 hPa, i.e. around -2×10^{-1} to -2.5×10^{-1} Pa s^{-1}), essentially due to advection terms (VA and LTA) and condensation and convective processes (LLH), as illustrated in Fig. 8a. The LSH induces weak upward motion below 930 hPa and sinking motion above this level. The friction effect reduces the total upward motion with a downward contribution around 850 hPa. In general, the diagnostic omega obtained via eq. (1) is in good agreement with the CRCM prognostic omega, despite an underestimation of diagnostic value near 800 hPa compared to the prognostic one.

Figure 8b shows that this upward motion is associated with a weak low-level cyclogenesis, with a close correspondance between the diagnostic obtained with eq. (3) and prognostic values and with only a quantitative difference below 970 hPa. At this point no cyclogenesis would occur below 800 hPa without diabatic forcings. The profile of vorticity tendency also suggests an increase in cyclogenesis between the surface and 900 hPa due to the convective processes. In fact, all the forcings are concentrated in the levels below 800 hPa, with a very weak contribution by vorticity advection in the upper troposphere associated with the short-wave trough (suggested in Fig. 3b 3 h after this profile).

The profiles of tendency of advection terms at point A at 0400 UTC 8 December are shown in Figs. 8c and 8d. As illustrated in Fig. 8c, the diagnostic of VA tendency obtained via eq. (15) and the prognostic issued from CRCM are quite similar. The tendency of vorticity advection is maximum at low levels (the maximum value appears around 950 hPa), essentially due to LSH and F below 900 hPa, and to the temperature advection between 980 and 920 hPa. Above 900 hPa the vorticity advection becomes negative due to the diabatic and thermal effects. At this moment turbulent fluxes of heat and momentum at 1000 hPa contribute substantially to the 1000-hPa increase of VA, in spite of the negative contribution by the VA forcing itself and the LLH term. At high levels the tendency of vorticity advection is weak above 700 hPa. This structure of vorticity advection change is very different from that of a classical mid-latitude cyclone, where this dynamic term (and consequently its tendency) is generally larger at high levels. Finally, we can anticipate that this increase of vorticity advection at low levels is a favorable factor for the deepening of the surface trough in this sector in the next 3 h.

Figure 8d shows that the diagnostic of LTA tendency obtained via eq. (17) is very similar to the prognostic value. At this moment the tendency of LTA is negative below 950 hPa and negligible higher up. This decrease of LTA is essentially due to the strong contribution by diabatic terms, especially the LSH, which dominate the thermal advection effect, as suggested in the horizontal distribution shown in Fig. 7. Hence the heat flux from the open water reduces the local maximum of cold air advection near the surface, which contributes to modify strongly the profile of temperature below 950 hPa. This modification is also favorable to the deepening of the surface trough in this sector in the next 3 h.

Figures 9a and 9b show the contributions to vertical motion and vorticity tendency at the same point A 3 h later, at 0700 UTC 8 December. The upward motion has slightly increased below 800 hPa (around -2.5×10^{-1} to -3.5×10^{-1} Pa s^{-1} at 830 hPa) from the last 3 h (compared to Fig. 8a). This increase is essentially due to the modification of temperature advection, which now contributes to the upward motion below 900 hPa. As was seen before in Fig. 8d, this modification in temperature advection is very shallow, being concentrated near the surface, but has a net effect on the low-level vertical motion. The other forcings have almost the same contribution as before. At the same time, the vorticity tendency has also increased below 800 hPa (Fig. 9b) and is twice as important at 1000 hPa (around 3.5×10^{-9}, compared to 1.7×10^{-9} s^{-2} 3 h before shown in Fig. 8b). As noted before, the

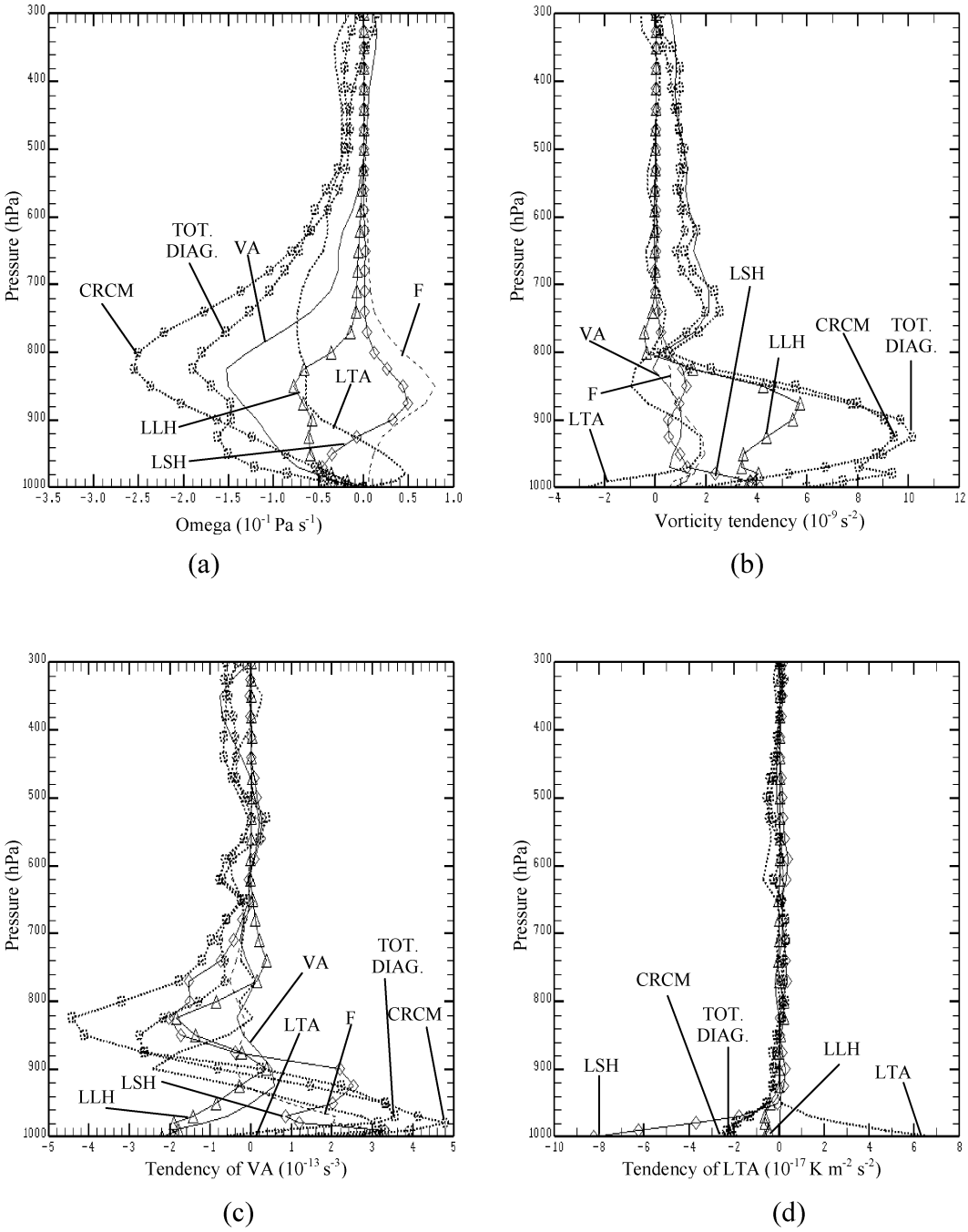

Fig. 8. Profile on pressure levels at point A (refer to Fig. 4a) at 0400 UTC 8 December: (a) prognostic and diagnostic vertical motions [cf. eq. (1)]; (b) prognostic and diagnostic vorticity tendencies [cf. eq. (3)]; prognostic and diagnostic tendencies of VA [cf. eq. (15)]; prognostic and diagnostic tendencies of LTA [cf. eq. (17)]. TOT. DIAG. refers to the contribution of all forcings.

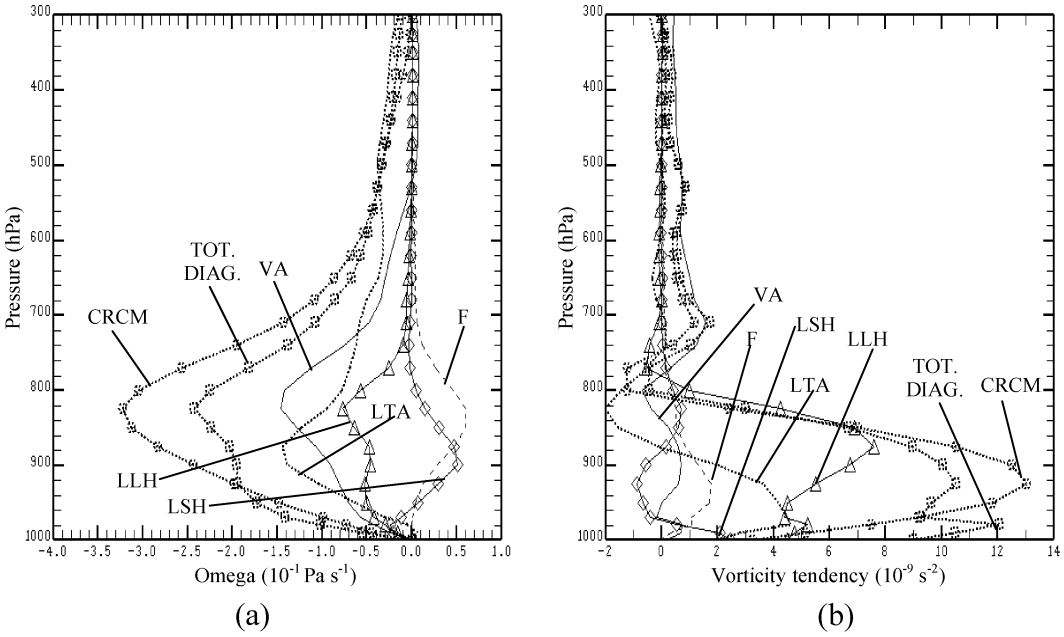

Fig. 9. Same as Fig. 8 (a and b for vertical motion and vorticity tendency, respectively), but at 0700 UTC 8 December 1988.

diagnostic value is overestimated below 970 hPa. The LTA now contributes to increasing the cyclogenesis below 900 hPa in spite of cold air advection. The VA contribution was maintained and stayed weak during this time. In fact, the LSH and F forcings, which have contributed to increasing the low-level vorticity advection (shown in Fig. 8c), have allowed a trough to be maintained in the vicinity of the surface, and hence are favourable to the quasi-constant contribution by the VA term for the low-level cyclogenesis. Without the contribution of the low-level turbulence, the VA term itself would reduce the low-level cyclogenesis at 0700 UTC 8 December. Furthermore, the growth in the low-level convection during the time has allowed an increase of the LLH forcing on the cyclogenesis, especially between 950 and 850 hPa. As before, the maximum cyclogenesis is not directly at the surface but at 930 hPa, where the convective, thermal and momentum effects are cumulated.

4.2.3. Spatial distribution of 1000-hPa vorticity tendency. Finally, Fig. 10 shows the spatial distribution of vorticity tendency at 1000 hPa at the same time as the profiles discussed in Fig. 9, i.e. at 0700 UTC 8 December. At this time, the surface cyclogenesis increases in the northwestern part, along the sea-ice edge, in the central part and along the eastern coastlines of Hudson Bay (Fig. 10a). In the northwestern part of the Bay the maximum deepening is located near the maximum warming over open water (as suggested previously 3 h before in Fig. 4a). As indicated in Fig. 10b, LSH induces cyclogenesis over open water along the sea-ice margin or coastline and anticylogenesis over sea ice where the LSH is positive (suggested in Fig. 5a 3 h before). This cyclogenesis is located in western and northern parts of Hudson Bay where cold air is advected, as is the cyclogenesis due to LLH (Fig. 10c). The vorticity tendency due to LTA is approximatively opposite to those of diabatic forcing, with anticyclogenesis over open water along the sea-ice limit and cyclogenesis over sea ice (Fig. 10d). Also, a band of cyclogenesis due to the formation of a discontinuity in thermal advection (as suggested before in LTA tendency) is co-located with the diabatic cyclogenesis along sea-ice margin in northwestern Hudson Bay. In the centre of the Bay, the vorticity tendency due to vorticity advection increases the cyclogenesis due to thermal forcing (Fig. 10e). The vorticity tendency due to friction is generally positive along the line of surface discontinuity and negative over sea ice or open ocean (Fig. 10f). However, a band of weak cyclogenesis extends from the northwestern sea-ice edge toward the centre of the Bay where the low-level wind shear, both

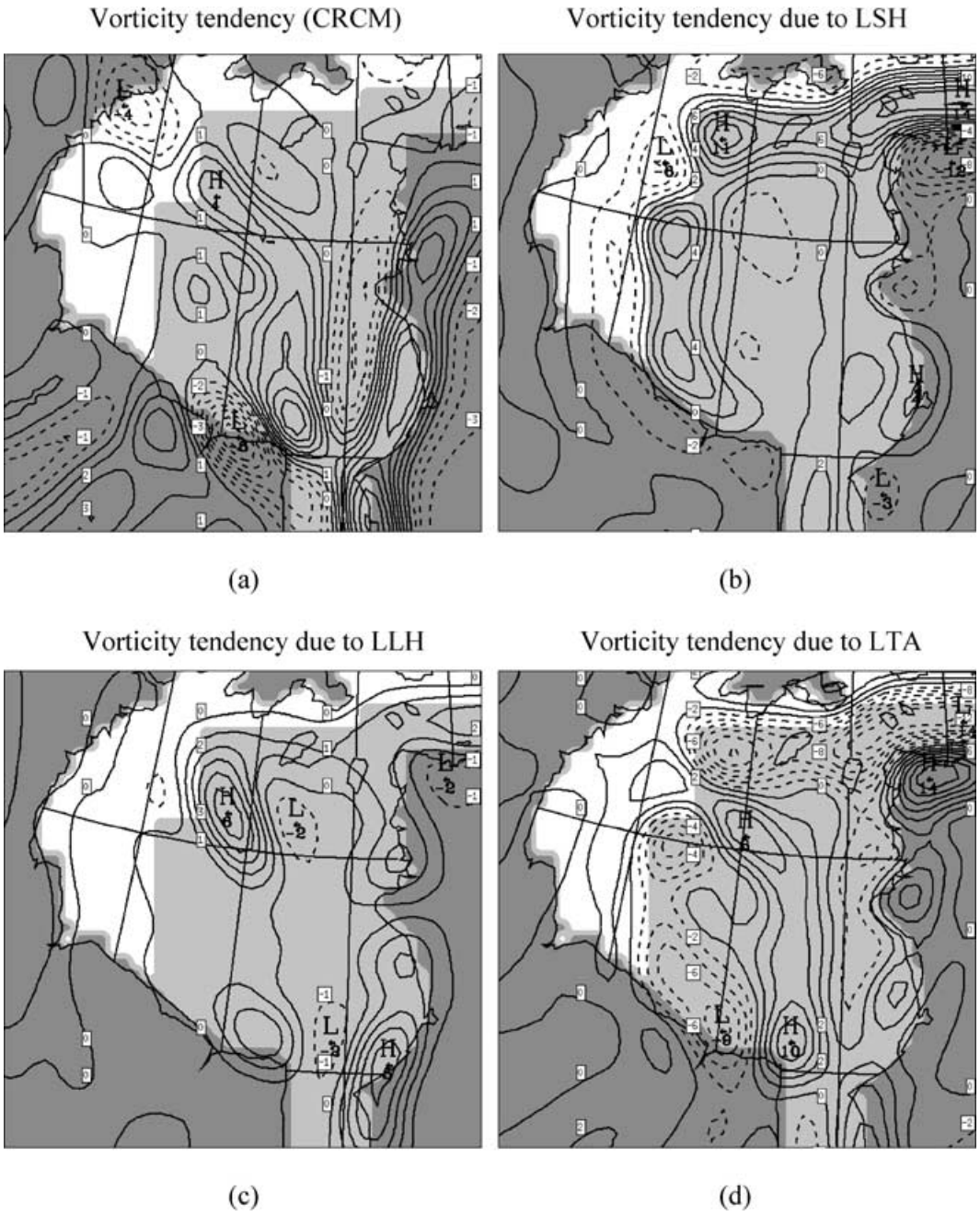

Fig. 10. 1000 hPa prognostic and diagnostic vorticity tendencies at 0700 UTC 8 December: (a) prognostic (every 2×10^{-9} s^{-2}); (b), (c), (d), (e) and (f) diagnostic due to LSH (every 2×10^{-9} s^{-2}), to LLH (every 1×10^{-9} s^{-2}), to LTA (every 2×10^{-9} s^{-2}), to VA (every 0.5×10^{-9} s^{-2}), and to F (every 0.5×10^{-9} s^{-2}), respectively.

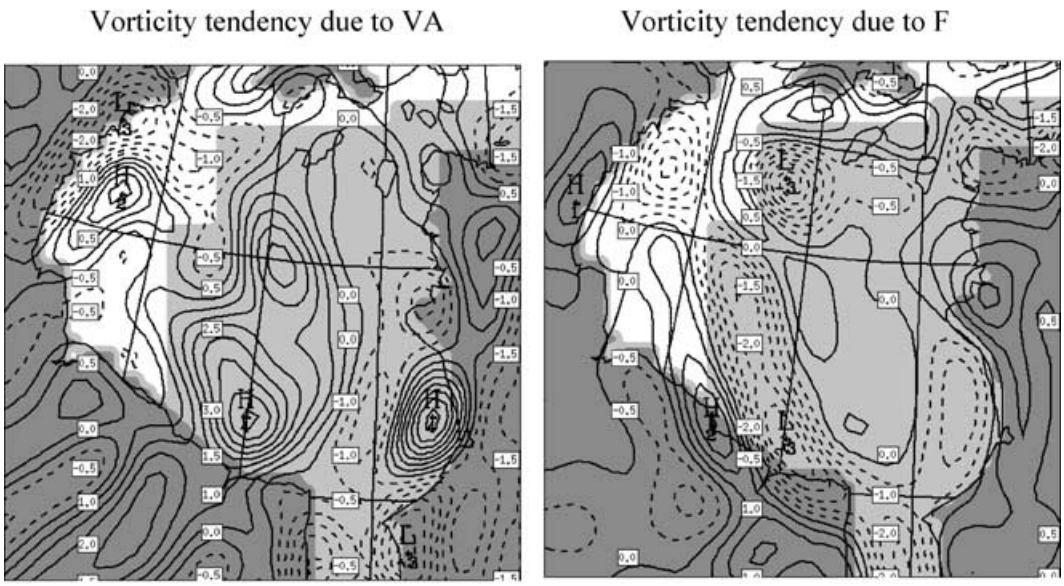

Fig. 10. (cont'd).

horizontal and vertical, is also important (not shown). Finally, as illustrated in the profile at point A (Fig. 9b), in the beginning of the polar low development, the sector of low-level maximum cyclogenesis is essentially due to the diabatic and thermal forcings, both over the northwestern and the eastern part of the Bay.

4.3. Direct effects of forcings on cyclogenesis during the mature stage

During the mature stage at 0700 UTC 9 December (shown in Fig. 3c), the polar low development is primarily due to the advection terms, which have reached their largest values, and dominant contributions for the vertical motion and low-level cyclogenesis. Figure 11 shows that the vertical motion and vorticity tendency are around four to five times more important than 12 h earlier. As suggested in Figs. 11a and 11b, the maximum in upward motion at 850 hPa is shifted toward the west of the maximum in surface cyclogenesis. At this time, strong upward motions (peak value of -14×10^{-1} Pa s^{-1}) occur in the offshore sector of the southwestern Hudson Bay. A long, broken belt of weaker upward motions is located toward the east and near the eastern shoreline. A sector of sinking motion occurs on the outer sides of the belts of ascent. The maximum of surface cyclogenesis (shown in Fig. 11b) is now located in southwestern Hudson Bay, with a maintenance of weaker cyclogenesis sector along the eastern shoreline.

As shown in Fig. 11c, in the region of maximum ascent, the upward motion is essentially due to VA, LLH and LTA in increasing order of relative importance. The convection is now fully developed up to 600 hPa, and the latent heat release and/or convective heat flux contributes around 30% of the total upward motion at 850 hPa. The vorticity advection contributes again to the low-level ascent, but the thermal advection now induces an upward motion at higher levels than before (essentially in the 900–650 hPa layer). Furthermore, the diagnostic and prognostic values of omega are quite similar.

As for vertical motion, the profile of vorticity tendency suggests that the cyclogenesis is realized on a thicker layer than at an earlier time, from the surface to 600 hPa (Fig. 11d). Unlike during the initial stage, when the diabatic and thermal terms were dominant and induced a maximum cyclogenesis at 920 hPa, now the cyclogenesis is maximum at the surface. This is primarily due to the cumulative effect of advection terms and the LSH below 950 hPa. LLH also allows the cyclogenesis to propagate above 850 hPa. The LTA

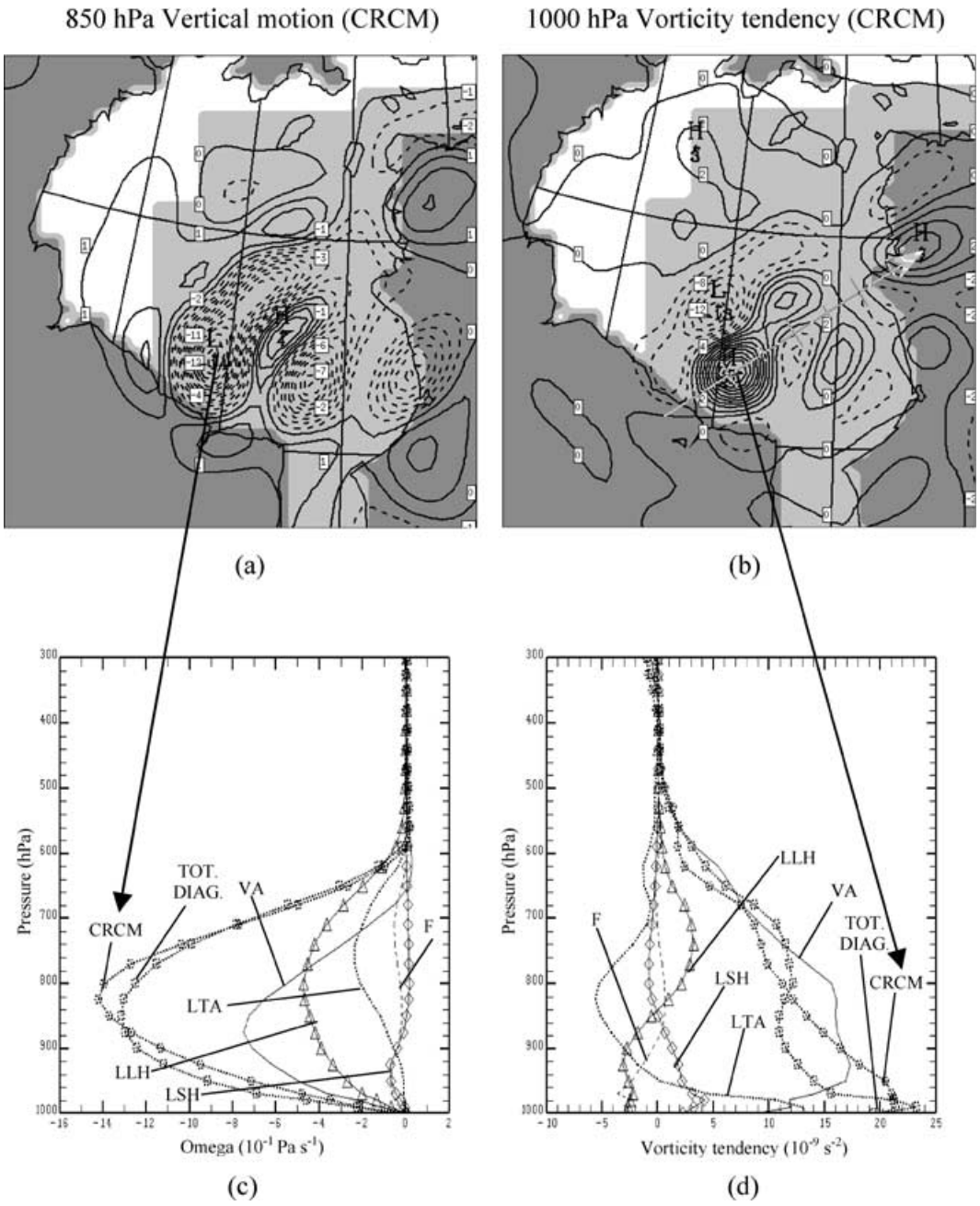

Fig. 11. Vertical motion and vorticity tendency at 0700 UTC 9 December 1988: (a) prognostic vertical motion at 850 hPa (every 1×10^{-1} Pa s^{-1}, dashed upward motion, solid downward motion); (b) prognostic vorticity tendency at 1000 hPa (every 2×10^{-9} s^{-2}); (c) and (d) profiles on pressure levels of vertical motion and vorticity tendency at point indicated by arrows (point of maximum values), respectively. Arrows (in gray) in panel (b) shows the location of the vertical cross-section in Fig. 12.

contributes again to the low-level cyclogenesis, but the vorticity advection acts from the surface to 500 hPa in association with the short-wave trough present in the upper level (shown in Fig. 3d). However, the presence of the low-level trough and maximum of vorticity advection below 800 hPa is essentially the result of the indirect effects via the turbulent, convective and thermal forcings as discussed in the previous subsection.

5. Discussion about the role of forcing interactions on polar low development

Because the above diagnostic analysis was limited to a single system, it cannot serve to formulate a general model of polar lows. For the system analysed here, however, we have determined the physical processes in a quantitative manner so as to obtain accurate estimates of the forcings and their interaction in polar low development. For this reason, we discuss in the next subsections the relative importance of each forcings for the direct and indirect effects studied above, and the general dynamics of this polar low.

5.1. Direct effects of forcings

The convergence of sensible heat flux over open water is the leading mechanism responsible for the warming of low-level continental cold air. This warming generates an increase of geopotential height over the heated zone, a pressure gradient favorable to anticyclogenesis and divergence above the heated layer, a decrease of surface pressure by mass continuity, surface convergence and an upward motion reaching its maximum in the middle of the heated layer. On the outer sides of the belt of warming appears a sector of low-level sinking motion and anticyclogenesis (shown in Fig. 10b). These effects of LSH on cyclogenesis and vertical motion are most intense along the sea-ice edge or coastline, where the surface heat fluxes are maximum, and change according to the position of the maximum low-level cold air advection.

The effects of latent heat release in organized deep convection and the convergence/divergence of convective heat flux act on cyclogenesis and vertical motion according to the deepening rate of the polar low (see Fig. 10c during the initial stage and Figs. 11c and 11d during the mature stage). These effects were essentially confined below 800 hPa during the initial stage and increased up to the level of 600 hPa during the mature stage. These correspond to the same kind of influence as that of the LSH, but with a more complex distribution during the life cycle of the polar low, according to the vertical structure and intensity of convection and condensation associated with the mesocyclone (see Fig. 12a for the effect on vertical motion during the mature stage).

Contrary to the diabatic effects, the low-level cold air advection has an opposite influence on divergence, pressure and vorticity tendencies, and vertical motion. However, this simple view must be nuanced, because the vertical structure of cold air advection determines the pattern of vertical motion and pressure tendency, not solely the horizontal feature of the LTA. Also as shown in Fig. 12b, during the mature stage, above the very shallow cold air advection from the surface to 950 hPa, a warm air seclusion was present aloft from 925 to 680 hPa and cold air advection above until 530 hPa (in association with the short-wave trough at 500 hPa shown in Fig. 3d). This structure of temperature advection induces a strong upward motion whose maximum is centered near the maximum of the warming layer and is shifted westward of the surface maximum cyclogenesis (see the position of the arrow in Fig. 12b). During the time of the deepening surface low, the thermal advection effect also increases at higher levels and becomes the main factor for the vorticity tendency and vertical motion, with the vorticity advection forcing. Also, the progressive warming by surface fluxes induces an increase in low-level cyclogenesis from the sea-ice–coastline boundary to offshore open water. Near the center of the surface trough, the LTA forcing is a dominant factor for polar low deepening, the track of which is organized by the sea-ice–coastline boundary from northwestern to southern Hudson Bay.

The low-level stress has a non-negligible effect on surface cyclogenesis along the sea-ice margin, as illustrated in Fig. 10f. Generally, strongest wind speeds are located along the sea-ice boundary or coastline near open water (not shown). Friction generates surface divergence near this surface discontinuity, favourable to surface pressure decrease and surface cyclogenesis, with weak subsident motion at low levels (see Figs. 8a and 8b). Conversely, toward open ocean, momentum flux near the surface creates surface convergence, upward motion at low levels and surface anticyclogenesis. As turbulent heat flux, the effects of surface stress are concentrated below 800 hPa where the wind shear is largest.

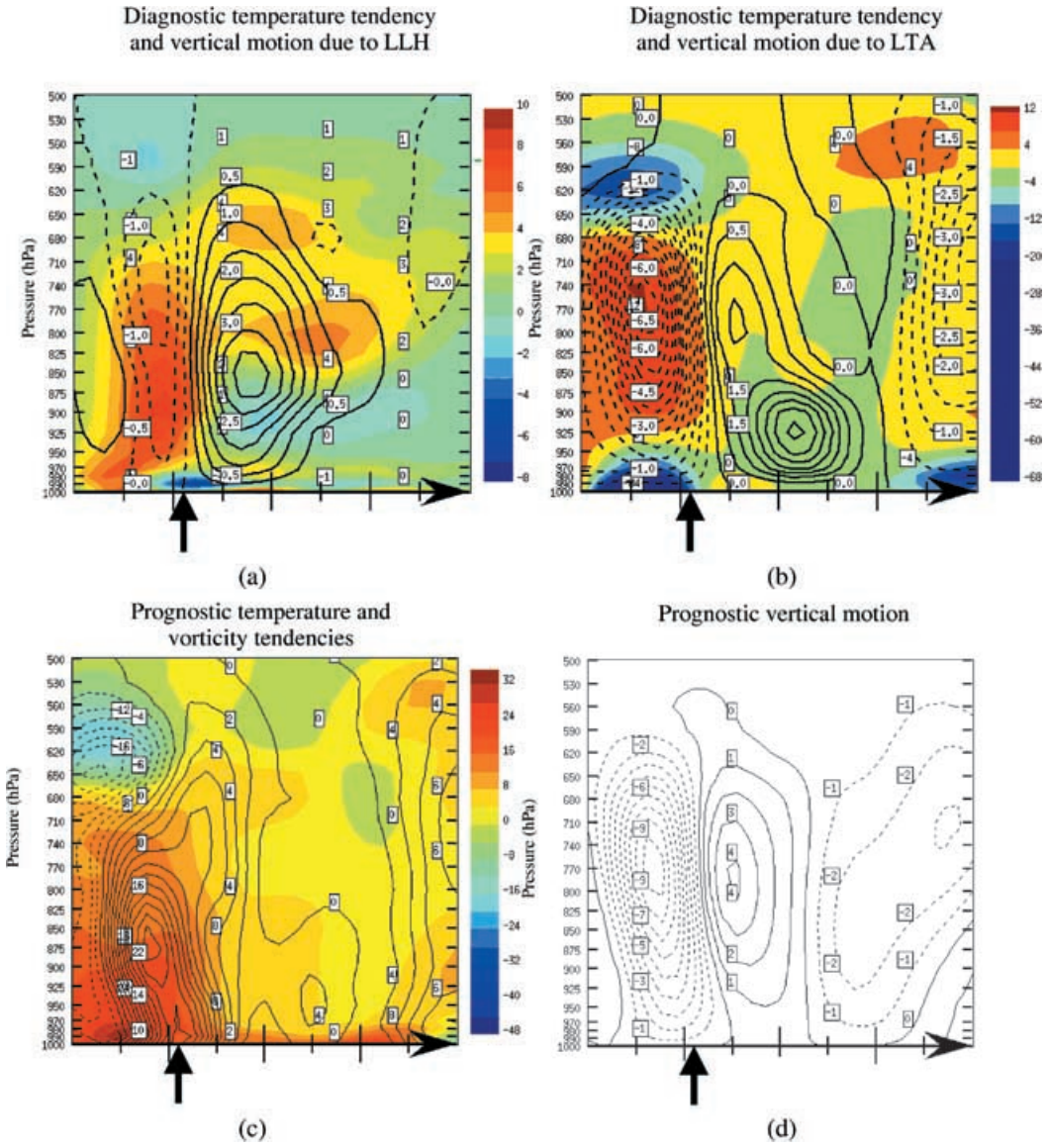

Fig. 12. Vertical cross-section (along baseline indicated in Fig. 11b) at 0700 UTC 9 December of (a) and (b) diagnostic temperature tendency (color scale every 1×10^{-5} or 4×10^{-5} K s^{-1}, for LLH or LTA, respectively) and vertical motion (every 0.5×10^{-1} Pa s^{-1}, dashed upward motion, solid downward motion) due to LLH and LTA forcings respectively, (c) prognostic temperature (color scale every 4×10^{-5} K s^{-1}) and Vorticity tendencies (every 2×10^{-9} s^{-2}, solid cyclogenesis, dashed anticyclogenesis), and (d) vertical motion (every 1×10^{-1} Pa s^{-1}, dashed upward motion, solid downward motion). Vertical axis is pressure (in hPa) and arrows at the bottom locate the maximum of cyclogenesis at 1000 hPa, where the profile has been realized in Fig. 11d.

The vorticity advection increases considerably at low levels during the deepening of the surface trough. It was regularly largest near the surface, between 900 and 800 hPa, where the turbulence and convective effects are most intense, and it induces a strong effect on cyclogenesis and vertical motion during the mature stage, as illustrated in Figs. 11d and 11c, respectively.

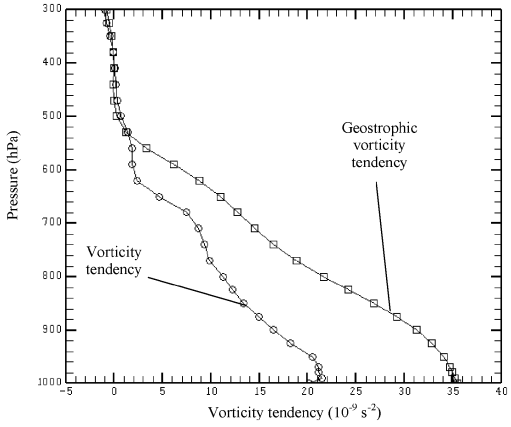

Fig. 13. Profile on pressure levels (in hPa) of prognostic vorticity tendency and geostrophic vorticity tendency (in 10^{-9} s^{-2}) at the same point as Fig. 11d. This figure reveals that, despite the difference in the low-level values of the vorticity tendency and its geostrophic counterpart, the vertical variation of these two tendencies is relatively similar (the slope of these two tendencies is quite similar).

5.2. Indirect effects of forcings

According to the low-level pressure changes generated by different forcings, the indirect effects of all terms are important for vorticity advection near the surface. For example, for LSH forcing, the pressure fall at the surface and the pressure increase above the heating layer tend to create a short-wave trough at the surface and a ridge aloft. This distribution of pressure changes due to LSH generates a negative zone of vorticity advection near the surface along sea-ice margin or coastline, and a positive zone of VA over open water, as exemplified in Fig. 6c. Above the heating layer, the distribution of vorticity advection tendency is opposite (in sign) and less intense because the pressure change due to LSH decreases with height. Obviously, all these effects depend on the depth and distribution of diabatic heating. For LLH forcing, these effects are similar but distributed over a thicker layer, and increase with time with the intensity of the active convective layer.

The effects of LTA on vorticity advection tendency are opposite to the LSH forcing ones, due to differences in pressure changes between these two forcings. This structure is not exactly co-located to the tendency of VA due to diabatic forcings, because temperature advection and diabatic heating zones are differently distributed spatially (especially in the vertical), as illustrated in Fig. 6e. However, as diabatic terms, the effects of LTA on VA tendency are strongly dependent on the pattern of source/sink of heat controlled by sea ice distribution. As other forcings, surface stress also generates a short-wave trough near the surface, in the vicinity of the sea-ice edge and coastline, as exemplified in Fig. 6g. Upstream of the axis of maximum surface cyclogenesis due to F, a negative tendency of VA is produced over sea-ice or continent and, downstream of this cyclogenesis axis, a positive VA tendency is generated over open water. This positive zone of VA was often co-located with diabatic forcings, as illustrated at point A in Fig. 8c, to the northwest of the polar low center.

For tendencies of LTA, diabatic forcings determine the distribution of temperature advection at low levels, with quasi-null effect by dynamic terms. In particular, the sensible heat flux tends to increase temperature gradients along the sea-ice edge in a context of cold air advection, and to decrease these gradients over open ocean. Consequently, due to these changes of temperature gradients, LSH increases LTA along the sea-ice margin or coastline and decreases LTA over open water, as shown in Fig. 7c. For the second diabatic forcing, the LLH near the surface or, in our case, the cooling due to divergence of convective heat flux at 1000 hPa, decreases the temperature gradients over open water along surface discontinuities (not shown). For all diabatic terms, the effects on LTA are concentrated along the sea-ice margin or coastline, in the region of the axis of the maximum atmospheric heating/cooling rate over open ocean.

In the course of time, temperature advection tends to shift the zone of large temperature gradients, generated by the sea-ice limit position, toward the open ocean (Fig. 7d). Consequently, this change of temperature gradient location corresponds to a decrease of LTA near the sea-ice edge and an increase of LTA over open water. These tendencies of LTA due to thermal forcing are closely superimposed and opposed to those associated with the diabatic terms. Where the discontinuities of surface heat flux are large, such as near a major indented shape of sea-ice, the cumulative effects of LTA changes can produce a strong variation of temperature advection and the formation of a discontinuity in the thermal advection Laplacian.

5.3. Polar low dynamic

In the initial stage of the polar low development, a surface trough tends to form in northwestern Hudson Bay due to direct effects of diabatic heat fluxes along

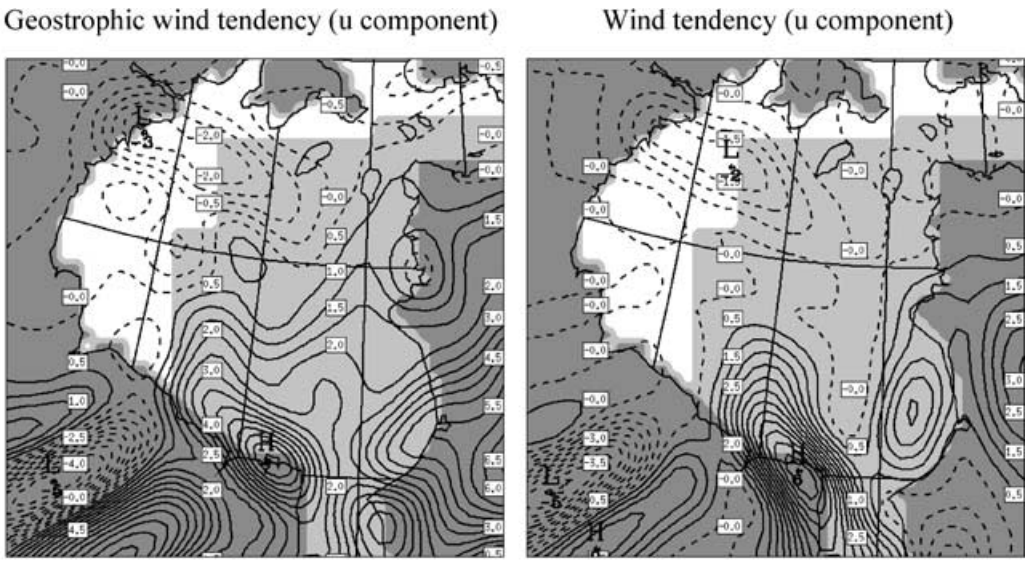

Fig. 14. 1000 hPa prognostic wind tendency (every 0.5×10^{-4} m s^{-2}) at the same time as Fig. 4: (a) and (b) are the geostrophic and real u component of the wind, respectively. This figure shows that the wind tendency and the geostrophic one are strongly correlated, and near the surface the wind tendency is smaller than the geostrophic counterpart.

the sea-ice edge. Near the indented sea-ice shape, the indirect effects combine to increase the surface deepening of the low and vertical motion via the simultaneous growth in the low-level vorticity advection and the decay in the Laplacian of thermal advection due to turbulent fluxes. In fact, along straight sea-ice margin, diabatic effects inducing cyclogenesis are opposite to thermal forcings because cold air advection generally contributes to anticyclogenesis. On the other hand, the non-rectilinear contour of the sea-ice edge modifies the distribution of maximum cold air advection via the discontinuity in source (or sink) of surface heat fluxes, which in turn induces a discontinuity in local thermal Laplacians. This then favors the establishment of net low-level air warming, and this spatial variation in thermal Laplacian constitutes a factor for local cyclogenesis. Hence, at the initial stage, the cylogenesis maximum is located near the sector of maximum low-level warming, just to the southeast of the indentation in sea-ice shape. Albright et al. (1995) have previously noted qualitatively that the straight-sea-ice limit is less favourable to cyclogenesis than an indented margin. In the experiments of Albright et al. (1995), the simulation with a straight-line ice boundary (their HB10 experiment) shows a considerably weaker cyclone and a more northerly position of the low center than the simulation with an indented ice limit (their HB9 experiment). Our experiment confirmed that the indented sea-ice limit not only amplifies the polar low development, but also modifies the cyclone track. These effects are primarily due to the low-level advection term changes associated with the surface heat, moisture and momentum flux distributions.

During the deepening of the cyclone and its migration toward the southwest in moving away from the ice edge, the mesocyclone deepens via the increase in advection and convective forcings. A low-level baroclinic structure (shown in Fig. 12c) was progressively developed due to the position of the maximum low-level warming, located along the ice/continent border (in the left of the arrow), and the maximum surface cyclogenesis situated offshore over open ocean (represented by the arrow), where the combined effect of all forcings is more effective. Figures 12c and 12d also reveal a tilt in the vertical, with a maximum cyclogenesis at 850 hPa and a maximum upward motion aloft at 770 hPa, westward of the maximum surface cyclogenesis. The baroclinic structure of this cyclone is also in agreement with the qualitative work of Mansfield (1974) and Montgomery and Farrell (1992). This

baroclinic system was developed on the downstream side of the maximum heating axis associated with surface heat fluxes, where the structure of temperature and vorticity advection leads the deepening more efficiently. This low-level baroclinic structure is the result of the distribution of diabatic heat fluxes associated with the pattern of the open water/sea-ice/coastline boundary.

The polar low has a warm core due to the turbulent and convective heat fluxes (see Fig. 12a for the effects of LLH on temperature tendency and vertical motion) and the temperature advection above 925 hPa (warm air seclusion above the low-level cold air advection, as illustrated in Fig. 12b). This recognized structure has been identified in other polar low studies (e.g. Grønås et al., 1987; Mailhot et al., 1996). Our polar low study confirms Mak's (1998) work, concerning the role of surface heat flux on the low-level formation of an unstable short-wave trough, with a shallow structure near the surface and a westward tilt with height.

Moreover, the momentum flux near the discontinuity in sea surface conditions could have an important effect on the low-level short-wave trough pattern, as suggested before by Branscome et al. (1989). Our study, however, shows that surface stress participates in cyclogenesis, contrary to the classical view of this forcing, which is often thought to inhibit surface cyclogenesis. This contribution is essentially indirect via the low-level increase of vorticity advection over open water.

As suggested by Albright et al. (1995), the cold low at upper level shown in Figs. 3d and 12c (see the negative temperature tendency between 650 and 530 hPa on the left-hand side of surface cyclogenesis) could amplify the surface low development with the combined effect of the low-level warming and moistening by surface fluxes (see the maximum upward motion in Fig. 12d above the heated layer, to the left of the arrow). However, in our case, this upper level cooling did not result in a deeper convection. Indeed, as revealed in Fig. 12a showing the temperature tendency and vertical motion due to LLH (weak maximum upward motion near 750 hPa), the condensation heating in deep convection were kept below 620 hPa. Furthermore, the temperature advection by itself, in particular the vertical structure with alternative cold, warm, and cold advection in the southwest of the surface low pressure, has induced a strong maximum upward motion near the maximum warming around 750 hPa. Yet, as shown in Fig. 11d, the vorticity advection alone induces a propagation of weak cyclogenesis from 600 to 500 hPa. Globally, however, during the moving of this upper-level cold low, the surface cyclogenesis has not increased significantly after this time. Consequently, the upper level cold trough appears to have played a secondary role in this polar low development, where the baroclinic structure at low levels was the necessary mechanism to spin up its development. Hence, the upper-level baroclinic forcing by itself was insufficient to initiate this shallow polar low, in agreement with the studies of Roch et al. (1991) and Albright et al. (1995).

6. Summary and conclusions

A 30-km version of the Canadian Regional Climate Model has been used to simulate a polar low development between 8 and 9 December 1988 over Hudson Bay. Diagnostic equations have been developed to quantify the interactions between the various forcing factors for this polar low evolution. This case represents a typical polar low associated with strong surface heat, humidity and momentum fluxes over open water of Hudson Bay, due to low-level cold air advection. The rapid development of this polar low is due to the spatial configuration of temperature advection and vertical diffusion of heat and momentum at low levels. First, the direct effects of thermal and diabatic forcings contributed to induce surface cyclogenesis near the sea-ice margin. Progressively, the indirect effects of all forcings accelerate the deepening of a low-level short-wave trough over northwestern Hudson Bay. At this time, the temperature advection structures near the surface are strongly modified by diabatic forcings, propicious to surface cyclogenesis. Synergetic effects due to forcing interactions increase low-level circulation, thus inducing an increase in advection below 700 hPa. At the mature stage, the advection terms became the main factors of cyclone intensification, but again under the influence of surface fluxes and the growth in deep convection. Finally, the polar low studied here is primarily the result of combined forcing interactions near the sea-ice edge, which are responsible for vorticity and thermal advection changes at low levels.

Our study confirms that a polar low is very sensitive to the sea surface conditions, in particular the accurate location of the sea-ice margin or shape of the sea-ice contour, as suggested in previous studies (Grønås et al., 1987; Langland and Miller, 1989; Nordeng et al., 1989; Roch et al., 1991; Albright et al., 1995; Mailhot et al., 1996). The shape of the sea ice is very important

because it inherently affects the pattern of low-level interactions between the surface forcings. Important discontinuities of sea surface conditions, such as indented shape of sea ice or coastline along open water, constitute a favourable factor for local cyclogenesis, because they induce the formation of discontinuities in thermal and diabatic Laplacians, which in turn favours vorticity and temperature advection changes at low levels. This can explain in part that a curved sea-ice margin or the contour of coastline near ice-free ocean in the Labrador Sea, Baffin Bay or Hudson Bay, is a favourable sector of mesoscale polar low development in a context of cold air outbreak over open water during winter, as numerous studies have illustrated (Mailhot et al., 1996; Roch et al., 1991; Albright et al., 1995; Hanley, 1993). As was illustrated, the prefered positions for polar low formation are not only determined, as suggested by Fett (1989), by the behavior of boundary layer fronts that are common near the ice edge, but also by the structure of advections term changes at low levels, influenced by turbulent surface fluxes.

In the type of polar low analyzed here, all forcings are largest near the surface, in particular vorticity advection. This characteristic is distinct from the classical structure of mid-latitude synoptic-scale cyclones in which the advection terms are generally larger at upper tropospheric levels. The low-level baroclinic pattern due to the distribution of diabatic and thermal forcings is also a triggering mechanism to polar lows, as previously suggested in different studies (Nordeng and Rasmussen, 1992; Reed and Duncan, 1987; Shapiro et al., 1989; Fett, 1989). However, as we have demonstrated, this low-level baroclinic structure is the direct result of the pattern and distribution of sea-ice cover.

Another interesting finding was the strong influence of turbulent surface stress on the surface cyclogenesis. The momentum flux did not constitute a systematically inhibiting process for the development. The indirect effects of friction on vorticity advection changes played an important role on vorticity advection growth near the surface, favourable to an intensification or a maintenance of the surface cyclogenesis, during all development stages.

In this study, the diagnostic method developed to analyze forcing interactions was useful for identifying physical connections between different forcings and therefore determining key factors of mesoscale cyclogenesis. This method constitutes an alternative technique to classical methods, such as potential vorticity or equations with quasigeostrophic approximations. With these common methods, it is impossible to identify forcing interactions without ambiguity and to analyze their role on cyclogenesis. In our method however, the diagnostic equations to study indirect effects must be further improved in order to complete the analysis of forcing interactions. In particular, it is important to develop a quantitative procedure to determine more completely the link between the geostrophic wind tendency and the non-geostrophic counterpart. In our diagnostic equations, the wind changes have been exclusively deduced from mass redistribution, and the divergent component of the wind was not taken explicitly into account in the calculation of total wind tendency. In an intensifying weather system, the divergent component of wind can become important, sometimes reaching the same order of magnitude as the rotational component. This factor can explain in part the noted discrepancies between advection term tendencies issued prognostically from CRCM and from the diagnostic equations. In the diagnostic equations, we assumed that the proportionality factor between geostrophic wind and total wind tendencies was the same for all forcings. In reality this is not true, because turbulence has a major effect on the formation of ageostrophic wind in the boundary layer, and it is certainly important to separate more completely the relative contribution of each forcing in wind tendency. This aspect of the diagnostic method must be improved in future work in order to realize a better agreement between diagnostic results and model outputs. Finally, in order to complete the study of forcing interactions, it is necessary to analyze the physical reasons for turbulent flux changes due to all terms. However, this is not an easy problem because the variation of turbulent fluxes are strongly nonlinear, dependent on stability, wind speed and roughness parameters. In spite of these limitations, the understanding of the role of forcing interactions in cyclone development has been improved with our new diagnostic method, in agreement with the suggestions of Kuo et al. (1991).

This type of cyclone development corresponds to a rapid and intense cyclogenesis, where forcings are confined in a thin layer near the surface. In particular, it has been demonstrated that the role of the shallow modification of horizontal temperature advection via surface heat fluxes on polar low development is the key factor of this type of mesocyclone formation. The structure of this mesocyclone is very sensitive to the distribution and intensity of turbulent and convective fluxes in the boundary layer. Hence, the simulated polar low depends strongly on the physical parameterizations in the model, and not only on the distribution of

sea surface conditions, as suggested by previous studies (Roch et al., 1991; Albright et al., 1995; Mailhot et al., 1996). The diagnostic method used in this study constitutes a tool not only to furthen our understanding of mesocyclogenesis, but also to validate and improve model physics.

7. Acknowledgments

Great thanks are due to Guy Bergeron, Michel Giguère and Christian Pagé for their help with the CRCM model runs and equations development. Thanks also are due to Claude Desrochers and Eva Monteiro for their role in the maintenance of computational systems at UQAM (University of Quebec at Montreal). Valuable discussions with Dr. Daniel Caya in the model configuration are gratefully acknowledged. This research has been able to benefit from financial support of NSERC (Natural Sciences and Engineering Research Council), the Meteorological Service of Canada through the Climate Research Network managed by the Canadian Institute for Climate Studies, UQAM's graduate scholarship, and PERD (Program on Energy Research and Development). We would also like to thank the two anonymous reviewers for their useful comments and valuable criticisms to improve this manuscript.

REFERENCES

Albright, M. D., Reed, R. J. and Ovens, D. W. 1995. Origin and structure of a numerically simulated polar low over Hudson Bay. *Tellus* **47A**, 834–848.

Bergeron, G., Laprise, R. and Caya, D. 1994. *Formulation du modèle de mésoéchelle compressible communautaire (MC2; Formulation of community compressible mesoscale model)*. Centre coopératif pour la recherche en mésométéorologie (CCRM), 165 pp, Bilingual Document. [Available from second author].

Branscome, L. E., Gutowski, W. J. Jr. and Stewart, D. A. 1989. Effect of surface fluxes on the nonlinear development of baroclinic waves. *J. Atmos. Sci.* **46**, 460–475.

Caya, D. 1996. *Le modèle régional de climat de l'UQAM (The Regional Climate Model of UQAM)*. Ph.D. Thesis, Université du Québec à Montréal, Montréal, Canada. 100 pp. [Available from second author].

Caya, D. and Laprise, R. 1999. A semi-implicit semi-lagrangian regional climate model: The Canadian RCM. *Mon. Wea. Rev.* **127**, 341–362.

Desjardins, S. 1993. *Étude diagnostique d'un front froid à l'aide de l'équation de développement de Zwack et Okossi version étendue utilisant les sorties du modèle régional aux éléments finis (Diagnostic study of a cold front with extended version of Zwack-Okossi equation using outputs of regional finite-element model)*. MSc Thesis, Université du Québec à Montréal, Montréal, Canada. 137 pp. [Available from third author].

Fett, R. W. 1989. Polar low development associated with boundary-layer fronts in the Greenland, Norwegian and Barents Seas. In: *Polar and Arctic lows*. (eds. P. F. Twitchell, E. A. Rasmussen, and K. L. Davidson). A. Deepak Publishing, Virginia, USA, 313–322.

Gachon, P. 1999. *Effets de la distribution de la glace marine sur le développement des dépressions à méso-échelle et sur le climat régional (Effects of the sea-ice distribution on mesoscale low pressure development and on regional climate)*. Ph.D. Thesis, Université du Québec à Montréal, Montréal, Canada. 352 pp. [Available from first author].

Gates, W. L. 1992. AMIP: The Atmospheric Model Intercomparison Project. *Bull. Am. Meteorol. Soc.* **73**, 1962–1970.

Grønås, S., Foss, A. and Lystad, M. 1987. Numerical simulations of polar lows in the Norwegian Sea. *Tellus* **39A**, 334–354.

Haltiner, G. J. and Williams, R. T. 1980. *Numerical prediction and dynamical meteorology*. Second edition, John Wiley & Sons, New York, 477 pp.

Hanley, D. E. 1993. *A case study of a polar low in the Labrador Sea.* MSc Thesis, Deptartment of Oceanography, Dalhousie University, Halifax, Canada. 165 pp.

Irbe, G. J. 1992. *Great lakes surface water temperature climatology, climatological studies*. Environment Canada, Atmospheric Environment Service, 43, 215 pp.

Kuo, Y. H., Low-Nam, S. and Reed, R. J. 1991. Effects of surface energy fluxes during the early development and rapid intensification stages of seven explosive cyclones in the western Atlantic. *Mon. Wea. Rev.* **119**, 457–476.

Langland R. H. and Miller, R. J. 1989. Polar low sensitivity to sea surface temperature and horizontal grid resolution in a numerical model. In: *Polar and Arctic lows,*. (eds. P. F. Twitchell, E. A. Rasmussen, and K. L. Davidson). A. Deepak Publishing, Virginia, USA, 247–254.

Ledrew, E. F. 1984. The role of local heat sources in synoptic activity within the Polar basin. *Atmos. Ocean* **22**, 309–327.

Mailhot, J., Hanley, D., Bilodeau, B. and Hertzman, O. 1996. A numerical case study of a polar low in the Labrador Sea. *Tellus* **48A**, 383–402.

Mak, M. 1998. Influence of surface sensible heat flux on incipient marine cyclogenesis. *J. Atmos. Sci.* **55**, 820–834.

Mansfield, D. A. 1974. Polar lows: The development of baroclinic disturbances in cold air outbreaks. *Quart. J. R. Meteorol. Soc.* **100**, 541–554.

McFarlane, N. A., Boer, G. J., Blanchet, J.-P. and Lazare, M. 1992. The Canadian Climate Centre Second Generation General Circulation Model and its equilibrum climate. *J. Clim.* **5**, 1013–1044.

MEP Company, 1989. *Polar lows in Canadian offshore waters*. Rep. MT 88250, available from Atmospheric Environment Service, Western Region, Edmonton, Alberta, Canada.

Montgomery, M. T. and Farrell, B. F. 1992. Polar low dynamics. *J. Atmos. Sci.* **49**, 2484–2505.

Morneau, G. 1995. *Sensibilité du calcul des flux de surface face à la résolution horizontale et temporelle d'un modèle atmosphérique (Sensitivity of calculation of surface fluxes on horizontal and temporal resolution of atmospheric model)*. MSc Thesis, Université du Québec à Montréal, Montréal, 94 pp. [Available from second author].

Nordeng, T. E. and Rasmussen, E. A. 1992. A most beautiful polar low. A case study of a polar low development in the Bear Island region. *Tellus* **44A**, 81–99.

Nordeng, T. E., Foss, A., Grønås, S., Lystad, M. and Mitbo, K. H. 1989. On the role of resolution and physical parameterization for numerical simulations of polar lows. In: *Polar and arctic lows*. (eds. P. F. Twitchell, E. A. Rasmussen, and K. L. Davidson). A. Deepak Publishing, Virginia, USA, 217–232.

Räisänen, J. 1997. Height tendency diagnostics using a generalized omega equation, the vorticity equation, and a nonlinear balance equation. *Mon. Wea. Rev.* **125**, 1577–1597.

Räisänen, J. 1995. Factors affecting synoptic-scale vertical motions: A statistical study using a generalized omega equation. *Mon. Wea. Rev.* **123**, 2447–2460.

Reed, R. J. and Duncan, C. N. 1987. Baroclinic instability as a mechanism for the serial development of polar lows: A case study. *Tellus* **39A**, 376–384.

Roch, M., Benoit, R. and Parker, N. 1991. Sensitivity experiments for polar Low forecasting with the CMC mesoscale finite-element model. *Atmos. Ocean* **29**, 381–419.

Saulesleja, A. 1986. *Great Lakes climatological atlas*. Canadian Government Publishing Centre, Environment Canada, AES, Ottawa, Canada. 145 pp.

Shapiro, M. A., Hampel, T. and Fedor, L. S. 1989. Research aircraft observations of an Arctic front over the Barents Sea. In: *Polar and arctic lows*. (eds. P. F. Twitchell, E. A. Rasmussen, and K. L. Davidson). A. Deepak Publishing, Virginia, USA, 279–290.

Tardif, R. 1992. *Estimation du mouvement vertical à l'aide des données en surface seulement: étude systématique et comparaison avec le mouvement vertical provenant d'un modèle numérique (Estimate of vertical motion with surface data only: Systematic study and comparison with vertical motion issued from numerical model)*. MSc Thesis, Université du Québec à Montréal, Montréal, Canada, 150 pp. [Available from third author].

Zwack, P., Pagé, C. and Tardif, R. 1996. *DIONYSOS: Un outil diagnostique d'étude des sorties des modèles numériques de prévision météorologique (DIONYSOS: a diagnostic tool for study the outputs of numerical forecast model)*. Internal Report of Groupe des Sciences de l'Atmosphère, Université du Québec à Montréal, Montréal, Canada, 35 pp. [Available from third author].